

# eROSITA-RU Tidal Disruption Events with Keck-I/LRIS: Sample Selection, Optical Properties, and Host Galaxy Demographics

Zirui Zhang<sup>1,2</sup>, Yuhua Yao<sup>3,1,4</sup>, Marat Gilfanov<sup>5,6</sup>, Sergey Sazonov<sup>5</sup>, Pavel Medvedev<sup>5</sup>, Georgii Khorunzhev<sup>5</sup>, Rashid Sunyaev<sup>5,6</sup>, Vikram Ravi<sup>7</sup>, S. R. Kulkarni<sup>7</sup>, Jean Somalwar<sup>1,4</sup>, Ryan Chornock<sup>1,4</sup>, Ilfan Bikmaev<sup>8</sup>, and Mark A. Gorbachev<sup>8</sup>

<sup>1</sup> Department of Astronomy, University of California, Berkeley, CA 94720-3411, USA

<sup>2</sup> College of Physics, Sichuan University, Chengdu, 610065, China

<sup>3</sup> Miller Institute for Basic Research in Science, 206B Stanley Hall, Berkeley, CA 94720, USA  
e-mail: yuhanya@berkeley.edu

<sup>4</sup> Berkeley Center for Multi-messenger Research on Astrophysical Transients and Outreach (Multi-RAPTOR), University of California, Berkeley, CA 94720, USA

<sup>5</sup> Space Research Institute (IKI), Russian Academy of Sciences, Profsoyuznaya 84/32, Moscow 117997, Russia

<sup>6</sup> Max-Planck-Institut für Astrophysik, Karl-Schwarzschild-Str. 1, D-85741 Garching, Germany

<sup>7</sup> Cahill Center for Astrophysics, California Institute of Technology, MC 249-17, 1200 E California Boulevard, Pasadena, CA 91125, USA

<sup>8</sup> Kazan Federal University, Kremlevskaya Str., 18, Kazan, 420008, Russia

## ABSTRACT

**Context.** We select seventy tidal disruption event (TDE) candidates among X-ray transients discovered during the eROSITA all-sky surveys in the Eastern Galactic hemisphere ( $0^\circ < l < 180^\circ$ ) between December 2020 and February 2022 (eRASS1–5).

**Aims.** We perform a systematic analysis of this sample to characterize the properties of their optical counterparts and host galaxies.

**Methods.** We cross-match each X-ray source to a host galaxy in archival optical surveys using Bayesian likelihood-ratio techniques and obtain Keck/LRIS spectroscopy for all 70 host galaxies. Host properties are inferred through SED fitting with Prospector and emission line analysis with pPXF. We develop a robust classification scheme using X-ray and broad line luminosities, narrow-line ionization diagnostics, and optical variability to identify high-confidence TDEs, for which we analyze optical spectral features, light curve properties, and host galaxy demographics.

**Results.** Our final sample contains 52 TDEs with redshifts of  $0.018 \leq z \leq 0.714$ , comprising 41 gold (high-confidence) and 11 silver (lower-confidence) events. The vast majority (93%) of gold TDEs are intrinsically brighter in the X-ray band, with  $L_{\text{X,peak}} > L_{\text{opt,peak}}$ . Among 23 events with detected optical flares, delayed X-ray peak is commonly observed. We identify transient spectral features in eight events, including six with prominent broad He II  $\lambda 14686$  and/or H $\alpha$  emission and two coronal-line TDEs. Host galaxy demographics reveal modest over-representation in green valley ( $\times 1.8$ ) and quiescent Balmer-strong ( $\times 5.3$ ) galaxies, significantly weaker than previous TDE samples, demonstrating greater diversity in star formation histories than previously recognized. Most TDE hosts exhibit suppressed star formation relative to the main sequence, consistent with X-ray selection biases against dusty star-forming galaxies.

**Key words.** Galaxies — Tidal disruption — X-ray transient sources — Supermassive black holes

## 1. Introduction

Tidal disruption events (TDEs) of stars by massive black holes (MBHs) produce a dazzling cornucopia of astrophysical phenomena. Accretion of stellar material gives rise to soft X-ray and extreme-ultraviolet (EUV) thermal flares (Komossa 2015). Re-processing of accretion emission and stream-disk shocks powers flares in the optical band (Andelman et al. 2022; Ryu et al. 2023; Price et al. 2024; Steinberg & Stone 2024). Relativistic jets are launched in  $\lesssim 1\%$  of events, resulting in spectacular radio and hard X-ray transients (Alexander et al. 2020; De Colle & Lu 2020). TDEs represent unique laboratories for studying MBH demographics (Stone et al. 2020; Yao et al. 2023; Hannah et al. 2025), as well as the accretion and jet physics of MBHs (Guo et al. 2024a; Yao et al. 2024).

The first observational evidence for TDEs came from the detection of soft X-ray flares from the centers of quiescent galaxies during the ROSAT (0.1–2.4 keV) all-sky survey (RASS)

in 1990–1991 (Bade et al. 1996; Komossa & Greiner 1999). Their X-ray luminosity was observed to increase over  $\sim 1$  month and decay over years, with the decline rate generally following the theoretically expected mass fall-back rate of  $\propto t^{-5/3}$  (Rees 1988; Phinney 1989). Subsequently, using RASS as a reference, the search for soft X-ray nuclear transients in the Chandra and XMM-Newton archives yielded  $\sim 20$  TDEs and TDE candidates (see Saxton et al. 2020 for a review).

Since  $\sim 2010$ , optical sky surveys have dominated the TDE discovery rate (see, e.g., Fig. 1.5 of Yao 2023). The continuum emission of these events is characterized by blackbody radiation with effective temperatures of  $\sim 20,000$  K. Depending on the presence or absence of broad emission lines around He II, He I, and the Balmer series, they are broadly classified into TDE-H, TDE-He, TDE-H+He, and TDE-featureless (van Velzen et al. 2021; Hammerstein et al. 2023). Within individual events, the evolution of relative line strengths is common, and transi-

tions between spectral subtypes are observed (Charalampopoulos et al. 2022). This spectroscopic diversity might be attributed to the stratified structure of line emitting region, where the effective photospheres of different lines arise from distinct layers. Lines can be broadened with electron scattering (Roth et al. 2016), bulk kinetic motion in optically thick outflow (Roth & Kasen 2018; Nicholl et al. 2020), or Keplerian rotation of a disk (Short et al. 2020).

Population studies of host galaxy properties of early optical TDE samples show that the host galaxies generally show low levels of current star formation (weak H $\alpha$  emission) and substantial star formation in the last  $\sim$  Gyr (strong H $\delta$  absorption) (Arcavi et al. 2014; French et al. 2016). These so-called quiescent Balmer-strong (QBS) or E+A galaxies appeared to dominate early TDE samples. More recent studies using the ZTF sample confirm this E+A/QBS over-representation, though the enhancement is less extreme than initially suggested (Hammerstein et al. 2021). In the galaxy color-mass diagram, optical TDEs occur preferentially in green valley galaxies, with rates exceeding those in both red sequence and blue cloud populations (van Velzen et al. 2021; Hammerstein et al. 2023; Yao et al. 2023).

A small subset of TDEs (probably those in gas-rich environments) exhibit prominent coronal emission lines and are referred to as CrL-TDE (Onori et al. 2022; Newsome et al. 2024; Callow et al. 2024; Clark et al. 2025). They form a subset of the population of extreme coronal line emitters (ECLEs; Komossa et al. 2008; Wang et al. 2011, 2012). These CrL-TDEs typically show accompanying X-ray or UV flares that ionize gas located well beyond the immediate disruption region, producing both the high-ionization coronal lines and reprocessed infrared (IR) emission (Jiang et al. 2021; Short et al. 2023; Newsome et al. 2024; Clark et al. 2025). As such, they are considered as light echos of TDEs. The star formation rates (SFRs) of the host galaxies of CrL-TDEs are statistically higher than that of other optically selected TDEs (Hinkle et al. 2024).

The X-ray discovery of TDEs experienced a renaissance from December 12 2019 to February 26 2022, when the eROSITA (0.2–8 keV; Predehl et al. 2021) telescope onboard the Spektrum-Roentgen-Gamma (SRG) mission (Sunyaev et al. 2021) was conducting all-sky surveys. Each eROSITA all-sky survey (eRASS) takes six months, with eRASS1–eRASS4 fully completed and nearly 40% of eRASS5 conducted before the telescope was put in safe mode. The 6-month survey cadence and the large grasp (product of field of view and effective area) of eROSITA allow for effective TDE search (Khabibullin et al. 2014). The selection of eROSITA TDE is independently performed by two consortia: eROSITA-RU for the eastern Galactic hemisphere ( $0^\circ < l < 180^\circ$ ) and eROSITA-DE for the western hemisphere ( $180^\circ < l < 360^\circ$ ). The first reports of TDEs candidates found by eROSITA began to appear soon after the start of the all-sky survey (Khabibullin et al. 2020b,a). Single-object studies have revealed various phenomena, from repeating nuclear transients consistent with partial disruptions (Liu et al. 2023) to TDEs with novel optical or X-ray properties (Yao et al. 2022; Malyali et al. 2023, 2024).

While individual discoveries have revealed the diversity of eROSITA TDEs, understanding the population as a whole requires uniform selection and statistical analysis. Such selection is challenging because, unlike most optically selected TDEs with characteristic broad emission lines, X-ray-selected (and optically faint) events must be distinguished from active galactic nuclei (AGN) that can produce similar soft X-ray flares (e.g., Brandt et al. 1995; Grupe et al. 1995), as witnessed by eROSITA (Medvedev et al. 2022; Khorunzhev et al. 2024; Grotova et al.

2025b). Despite these challenges, both eROSITA consortia have released TDE samples that probe population-level properties. From the eROSITA-RU side, Sazonov et al. (2021) presented 13 TDEs that were undetected in eRASS1 but appeared in eRASS2 at flux levels exceeding more than ten times the upper limits of eRASS1, with follow-up optical spectroscopy confirming their non-AGN nature. Khorunzhev et al. (2022) presented an additional sample of 5 TDEs detected by eROSITA in eRASS1–eRASS4 and confirmed by optical spectroscopy. From the eROSITA-DE side, Grotova et al. (2025a) reported 31 TDEs selected for X-ray variability amplitudes greater than four between eRASS1 and eRASS2, among which 11 sources have only photometric redshifts. Together, these studies established some key results: (1) the volumetric rate of X-ray TDEs is comparable to that of optically selected events, (2) X-ray TDE hosts are, like optical TDEs, preferentially found in green-valley galaxies, and (3) the majority of X-ray selected TDEs are intrinsically faint in the optical.

A much larger eROSITA TDE sample, with detailed characterization of both transient properties and host galaxies, is essential to address several outstanding questions. First, volumetric rates remain poorly constrained. Integrating the best-fit X-ray luminosity functions from Sazonov et al. (2021) and Grotova et al. (2025a) above the peak luminosities of  $L_X > 10^{42.5}$  erg s $^{-1}$  yields TDE rates that differ by a factor of four:  $\approx 204_{-104}^{+113}$  Gpc $^{-3}$  yr $^{-1}$  from Sazonov et al. (2021) versus  $\approx 52 \pm 15$  Gpc $^{-3}$  yr $^{-1}$  from Grotova et al. (2025a). As noted by Mondal & French (2025), the eROSITA-DE sample is probably contaminated by AGN due to its lower detection threshold. Second, existing eROSITA studies have not yet examined how TDE rates vary with host galaxy stellar mass or black hole mass. Such constraints are essential for using TDE samples to probe black hole mass functions and loss cone physics. Finally, potential correlations between UV/optical broad-line properties and X-ray loudness offer powerful diagnostics to distinguish between competing models of the TDE radiative emission mechanisms (Roth et al. 2020), but remain largely unexplored.

In this paper, we present optical spectroscopic observations using the Low Resolution Imaging Spectrometer (LRIS; Oke et al. 1995) on the Keck I telescope of 70 TDE candidates identified by the eROSITA-RU consortium. For most candidates, the Keck/LRIS spectra show only host galaxy light, with transient features detected in a small subset. We note that the 13 TDEs published by Sazonov et al. (2021) are all observed by LRIS, and are therefore included here for both comparison and completeness. These observations provide a comprehensive spectroscopic dataset for studying the host galaxies of TDEs.

The remainder of this paper is organized as follows. In Section 2, we outline the sample selection and host galaxy association procedures. Section 3 describes the archival photometry of the host galaxies and our new Keck/LRIS spectroscopic observations. In Section 4, we combine spectroscopy and photometry to derive host galaxy properties, address AGN contamination, and define a gold sample of the most robust TDEs. Finally, we discuss our findings in Section 5 and summarize in Section 6.

All coordinates are given in J2000. Optical observations are corrected for Galactic extinction using the Schlegel et al. (1998) dust maps and the Cardelli et al. (1989) extinction curves with  $R_V = 3.1$ . We adopt a standard  $\Lambda$ CDM cosmology with matter density  $\Omega_M = 0.3$ , dark energy density  $\Omega_\Lambda = 0.7$ , and the Hubble constant  $H_0 = 70$  km s $^{-1}$  Mpc $^{-1}$ . Unless otherwise noted, the uncertainties quoted represent 68% confidence intervals.

## 2. Initial Sample Selection

### 2.1. X-ray Selection

We selected TDE candidates from strongly variable X-ray sources detected by eROSITA-RU sky surveys in the 0.3–2.3 keV energy band (Medvedev et al. 2022). The source catalog was built and maintained by the eROSITA-RU X-ray source catalog science working group at the Space Research Institute (Moscow, Russia). As data from successive sky scans was collected throughout the mission, the master catalog was being updated and multiple selections were created to support various multiwavelength follow-up programs, including the extensive TDE identification campaign reported here. Selection criteria for TDE candidates evolved throughout the mission. The distribution of TDE candidates among participating optical telescopes also varied throughout the mission. Therefore the sample with Keck spectroscopy presented here is not statistically well-defined and is not a result of uniform selection across eROSITA sky scans. This data set should therefore be regarded as a large subsample of the full eROSITA TDE sample, which will be defined using strict and uniform criteria and presented in a future publication.

Prior to the end of 2022, we classified an X-ray source as highly variable if the source was not detected in the previous surveys and its flux in the 0.3–2.3 keV energy band during some eROSITA scan exceeded its upper limit in the previous scan by a factor of larger than  $R_{X,\min}$ . Our initial TDE candidate samples used  $R_{X,\min} = 10$  (Sazonov et al. 2021), later expanded to  $R_{X,\min} = 7$  to include fainter events (Khorunzhev et al. 2022). At the later stages of the mission we redefined the sample using the formalism described in Medvedev et al. (2022), which uses theoretical probability distribution for the flux ratio to select sources variable with the factor larger than  $R_{X,\min}$  at the specified confidence level (usually corresponding to  $3\sigma$ ). The sample with Keck spectroscopy presented here was largely selected using the former method with  $R_{X,\min} = 10$  and 7. Note that we do not use X-ray spectral softness in selecting TDE candidates among eROSITA extragalactic transients, as some TDEs are known to exhibit relatively hard spectra (e.g., Wevers 2020; Yao et al. 2022; Guolo et al. 2024a; Ho et al. 2025).

Our selection process applies several filters to distinguish TDE candidates from other types of Galactic and extragalactic transients, following the procedures described in Sazonov et al. (2021) and Khorunzhev et al. (2022). Specifically, we exclude Galactic sources based on positional coincidence (with the eROSITA 98% localization radius  $r_{98}$ ) with stars having statistically significant Gaia parallax and/or proper motion (Gaia Collaboration et al. 2023). We also exclude known and candidate AGN based on mid-infrared colors  $W1 - W2 > 0.8$  (Stern et al. 2012) in the WISE all-sky survey (Cutri et al. 2021), archival X-ray detections, or optical transients with AGN-like stochastic variability. These criteria evolved slightly (in particular, we used a stricter infrared-color condition,  $W1 - W2 < 0.5$ , in Sazonov et al. 2021) over the course of our TDE search; full details will appear in the forthcoming comprehensive catalog paper.

### 2.2. Host Galaxy Association

We identified the host galaxies of our TDE candidates as optical sources detected in the Panoramic Survey Telescope and Rapid Response System Data Release 1 (PS1; Flewelling et al. 2020). For regions outside the PS1 footprint, we used sources detected in the DESI Legacy Imaging Survey (LS; Dey et al.

2019) DR10. For PS1, we consider only objects classified as ‘GALAXY’ or ‘UNSURE’ by the machine learning catalog of Beck et al. (2021), and that have an  $i$ -band PSF magnitude. We assume that all TDE candidates are located at galaxy centers and are not associated with off-nuclear MBHs.

We cross-matched eROSITA sources with optical objects using a search radius of  $8\sigma_{\text{pos}}$  (note that  $r_{98} = 2.8\sigma_{\text{pos}}$ ). For each match, we computed the reliability  $R$  of the association using the Bayesian likelihood ratio method (Sutherland & Saunders 1992). We adopted a flat prior on the magnitude distribution of true associations and modeled the surface density of the background sources as  $dN/dm \propto m^{0.6}$ , as expected in a simple Euclidean universe with uniform spatial distribution.

For all optical objects with  $R > 0.1$ , we performed forced photometry using the Zwicky Transient Facility (ZTF; Bellm et al. 2019; Graham et al. 2019; Masci et al. 2019, 2023) and the Asteroid Terrestrial-impact Last Alert System (ATLAS; Tonry et al. 2018; Smith et al. 2020; Shingles et al. 2021). If a significant optical flare is detected near the time of the X-ray transient, we set  $R = 1$ . Optical spectroscopy (see §3.2) is obtained for X-ray sources with a unique optical counterpart having  $R > 0.9$ . We exclude Galactic sources and obvious broad-line AGN (BLAGN) whose optical spectra exhibit very strong broad emission lines (hydrogen Balmer series, Mg II, etc.) that significantly exceed the continuum level.<sup>1</sup> This yields a final sample of 70 TDE candidates with high-confidence optical associations. This sample, listed in Tables 1 and 2, is the focus of our analysis. We show the  $25'' \times 25''$  cutouts of the host galaxy associations in Appendix A. Of the 70 optical counterparts, 69 lie within the  $r_{98}$  region, while 1 (1.4%) lies outside, consistent with the 2% of counterparts expected to fall outside  $r_{98}$  by construction.

## 3. Data

### 3.1. Archival Photometry

We compiled UV-to-IR photometry for all host galaxies, adopting measurements with signal-to-noise ratio ( $S/N > 3$ ) as detections and  $3\sigma$  upper limits otherwise. UV fluxes were measured from the Galaxy Evolution Explorer (GALEX; Martin et al. 2005) using gPhoton (Million et al. 2016), with Kron apertures and optimized background annuli. For the optical band, we prioritized PS DR2 *grizy* Kron magnitudes (Chambers et al. 2016) where available, otherwise using the Sloan Digital Sky Survey (SDSS) DR16 (Stoughton et al. 2002). Near-infrared  $JHK_s$  magnitudes were drawn from the Two Micron All-Sky Survey (2MASS) extended source catalog (Skrutskie et al. 2006) where available. For the mid-infrared, we used data provided by the Wide-field Infrared Survey Explorer (WISE; Wright et al. 2010). We prioritized WISE photometry from the LS DR10 Tractor catalog (Nikutta et al. 2020), supplemented by LS DR10 aperture fluxes or entries from the AllWISE (Cutri et al. 2013) and CatWISE (Eisenhardt et al. 2020) catalogs.

### 3.2. Optical Spectroscopy

We obtained optical spectroscopy for the host galaxies of all TDE candidates using LRIS. For the blue side, we used the 400/3400 grism with a  $1''$  slit for all but four observations. SRGe J071310.4+725627 (ID 20) was observed with the 600/4000 grism and a  $1.5''$  slit. SRGe J174505.5+104700 (ID 55), SRGe J201138.9-210935 (ID 63), and the +1333-day spectrum of

<sup>1</sup> We later remove BLAGN with weaker broad lines in §4.3.3.

**Table 1:** List of eROSITA TDE candidates with unique reliable host galaxy association.

| ID | Name                  | $\alpha_X$ | $\delta_X$ | $r_{98}$ ('') | $\alpha_{\text{opt}}$ | $\delta_{\text{opt}}$ | $\Delta_{\text{pos}}$ ('') | $f_{X\text{peak}}$ | $t_{X\text{peak}}$ |
|----|-----------------------|------------|------------|---------------|-----------------------|-----------------------|----------------------------|--------------------|--------------------|
| 1  | SRGe J003524.8-263550 | 8.853195   | -26.597256 | 6.22          | 8.85251               | -26.59819             | 4.02                       | 31.32              | 2021-12-14.17      |
| 2  | SRGe J004123.2-153705 | 10.346576  | -15.618171 | 7.67          | 10.346609             | -15.618729            | 2.01                       | 26.12              | 2021-06-16.71      |
| 3  | SRGe J010301.0-130120 | 15.754132  | -13.022233 | 5.0           | 15.75312              | -13.021384            | 4.68                       | 69.01              | 2021-12-26.09      |
| 4  | SRGe J010445.8+044319 | 16.190908  | 4.721981   | 7.01          | 16.189389             | 4.722495              | 5.76                       | 20.3               | 2022-01-02.60      |
| 5  | SRGe J011603.1+072258 | 19.013054  | 7.382774   | 5.85          | 19.012677             | 7.382249              | 2.32                       | 32.55              | 2021-07-04.87      |
| 6  | SRGe J011943.5-024142 | 19.931051  | -2.695102  | 6.55          | 19.930647             | -2.696627             | 5.68                       | 16.26              | 2021-07-01.62      |
| 7  | SRGe J013204.4+122235 | 23.018508  | 12.376507  | 5.77          | 23.018675             | 12.376562             | 0.62                       | 22.2               | 2020-07-08.99      |
| 8  | SRGe J015353.9+372945 | 28.474627  | 37.495725  | 6.17          | 28.475665             | 37.496032             | 3.16                       | 10.36              | 2021-07-30.11      |
| 9  | SRGe J015444.7-070012 | 28.686206  | -7.0033    | 10.57         | 28.68661              | -7.003443             | 1.53                       | 14.87              | 2021-07-11.67      |
| 10 | SRGe J015754.6-154214 | 29.477387  | -15.704019 | 6.21          | 29.477263             | -15.70359             | 1.6                        | 26.15              | 2021-01-02.88      |
| 11 | SRGe J015907.1-150323 | 29.779444  | -15.05652  | 5.52          | 29.779383             | -15.056262            | 0.95                       | 24.16              | 2021-01-03.46      |
| 12 | SRGe J021213.6+310535 | 33.056503  | 31.093126  | 7.08          | 33.056536             | 31.092021             | 3.98                       | 14.85              | 2020-08-02.07      |
| 13 | SRGe J021939.7+361819 | 34.915471  | 36.305141  | 5.0           | 34.916264             | 36.305054             | 2.32                       | 24.7               | 2020-08-08.36      |
| 14 | SRGe J023017.3+283606 | 37.572164  | 28.601784  | 5.0           | 37.571364             | 28.601323             | 3.02                       | 84.78              | 2022-02-02.19      |
| 15 | SRGe J023440.1-021812 | 38.667082  | -2.303241  | 5.0           | 38.667078             | -2.302912             | 1.18                       | 43.86              | 2021-07-25.13      |
| 16 | SRGe J025548.1+142800 | 43.950595  | 14.466526  | 5.0           | 43.950275             | 14.466619             | 1.16                       | 104.64             | 2022-02-03.68      |
| 17 | SRGe J030747.8+401842 | 46.949092  | 40.311655  | 5.0           | 46.949274             | 40.311363             | 1.16                       | 726.75             | 2021-08-17.03      |
| 18 | SRGe J050948.4+695221 | 77.451697  | 69.872474  | 5.97          | 77.451198             | 69.872119             | 1.42                       | 19.58              | 2021-09-22.10      |
| 19 | SRGe J060324.7+621112 | 90.853098  | 62.18658   | 5.0           | 90.853499             | 62.186385             | 0.97                       | 82.46              | 2021-03-30.14      |
| 20 | SRGe J071310.4+725627 | 108.293384 | 72.940741  | 5.0           | 108.293835            | 72.940751             | 0.48                       | 112.16             | 2020-10-11.89      |
| 21 | SRGe J081006.4+681755 | 122.526835 | 68.298718  | 5.42          | 122.525923            | 68.299092             | 1.81                       | 23.2               | 2021-04-14.56      |
| 22 | SRGe J083640.9+805410 | 129.170469 | 80.902719  | 5.42          | 129.17618             | 80.903218             | 3.71                       | 19.54              | 2021-10-11.09      |
| 23 | SRGe J091747.3+524818 | 139.447148 | 52.805055  | 5.51          | 139.447492            | 52.805635             | 2.22                       | 26.39              | 2020-10-29.15      |
| 24 | SRGe J095928.7+643024 | 149.869625 | 64.50679   | 5.0           | 149.869012            | 64.506081             | 2.72                       | 44.04              | 2020-10-28.89      |
| 25 | SRGe J113323.2+693635 | 173.346493 | 69.60971   | 6.9           | 173.349376            | 69.609137             | 4.16                       | 13.52              | 2021-05-04.90      |
| 26 | SRGe J131014.7+444319 | 197.561406 | 44.72182   | 6.45          | 197.562712            | 44.72188              | 3.35                       | 22.67              | 2021-06-07.23      |
| 27 | SRGe J131404.1+515427 | 198.517088 | 51.907552  | 6.24          | 198.517527            | 51.907817             | 1.36                       | 24.99              | 2021-12-04.91      |
| 28 | SRGe J132718.1+350437 | 201.825359 | 35.076816  | 5.0           | 201.825306            | 35.076286             | 1.91                       | 42.59              | 2021-06-17.72      |
| 29 | SRGe J133053.5+734823 | 202.722784 | 73.806298  | 5.34          | 202.720918            | 73.806739             | 2.46                       | 24.75              | 2020-11-03.46      |
| 30 | SRGe J133731.5+601849 | 204.381115 | 60.313748  | 6.07          | 204.380151            | 60.313456             | 2.01                       | 13.65              | 2020-11-26.16      |
| 31 | SRGe J135353.7+535949 | 208.473873 | 53.996971  | 5.0           | 208.474197            | 53.997141             | 0.92                       | 140.46             | 2021-06-07.15      |
| 32 | SRGe J135515.0+311605 | 208.812591 | 31.267931  | 5.13          | 208.812579            | 31.268121             | 0.68                       | 38.35              | 2020-06-23.85      |
| 33 | SRGe J135812.1+195357 | 209.550215 | 19.899209  | 6.87          | 209.550684            | 19.898775             | 2.23                       | 20.35              | 2020-12-31.88      |
| 34 | SRGe J144738.3+671818 | 221.909782 | 67.305102  | 5.0           | 221.912771            | 67.305094             | 4.15                       | 62.54              | 2021-05-21.74      |
| 35 | SRGe J145226.6+670437 | 223.111019 | 67.076826  | 6.1           | 223.111719            | 67.076509             | 1.51                       | 7.51               | 2021-05-22.57      |
| 36 | SRGe J150328.1+495117 | 225.86706  | 49.854703  | 5.34          | 225.867028            | 49.853579             | 4.05                       | 11.68              | 2020-12-27.20      |
| 37 | SRGe J152656.3+353317 | 231.734534 | 35.554619  | 7.85          | 231.734127            | 35.553842             | 3.04                       | 9.68               | 2021-01-17.12      |
| 38 | SRGe J153134.9+330539 | 232.895476 | 33.094222  | 5.13          | 232.895722            | 33.094928             | 2.65                       | 19.92              | 2020-07-28.18      |
| 39 | SRGe J153331.5+390536 | 233.381222 | 39.093288  | 6.47          | 233.381985            | 39.092769             | 2.83                       | 12.57              | 2021-01-16.61      |
| 40 | SRGe J153403.5+621851 | 233.514553 | 62.314238  | 5.52          | 233.514195            | 62.314555             | 1.29                       | 16.71              | 2021-12-15.06      |
| 41 | SRGe J153503.3+455054 | 233.7639   | 45.848311  | 5.0           | 233.763172            | 45.848598             | 2.1                        | 34.21              | 2020-07-14.69      |
| 42 | SRGe J155113.5+515845 | 237.806284 | 51.979265  | 6.62          | 237.805954            | 51.978777             | 1.9                        | 6.26               | 2021-01-08.03      |
| 43 | SRGe J155834.0+382528 | 239.641788 | 38.424573  | 5.0           | 239.641623            | 38.424662             | 0.56                       | 18.02              | 2021-08-02.65      |
| 44 | SRGe J160943.1+253603 | 242.429451 | 25.600825  | 5.0           | 242.429019            | 25.601028             | 1.58                       | 23.05              | 2021-08-26.16      |
| 45 | SRGe J161001.3+330120 | 242.505597 | 33.022304  | 6.45          | 242.50592             | 33.022416             | 1.06                       | 14.12              | 2020-08-15.89      |
| 46 | SRGe J161559.1+360156 | 243.996068 | 36.032235  | 5.0           | 243.995909            | 36.031732             | 1.87                       | 32.26              | 2021-08-11.06      |
| 47 | SRGe J162159.4+271133 | 245.497537 | 27.192442  | 5.0           | 245.497951            | 27.192419             | 1.33                       | 19.95              | 2020-08-24.39      |
| 48 | SRGe J162932.1+280521 | 247.383633 | 28.089035  | 5.0           | 247.38332             | 28.08869              | 1.59                       | 53.06              | 2022-02-18.16      |
| 49 | SRGe J163030.3+470125 | 247.626092 | 47.023546  | 5.0           | 247.626052            | 47.02373              | 0.67                       | 32.22              | 2020-08-10.55      |
| 50 | SRGe J163831.9+534018 | 249.632855 | 53.671541  | 5.0           | 249.633401            | 53.672931             | 5.14                       | 15.22              | 2020-08-04.97      |
| 51 | SRGe J165055.8+301634 | 252.732698 | 30.275976  | 6.4           | 252.732439            | 30.275924             | 0.83                       | 15.1               | 2021-02-20.95      |
| 52 | SRGe J170139.0-085911 | 255.412324 | -8.986521  | 6.06          | 255.412083            | -8.98657              | 0.87                       | 23.49              | 2021-03-13.86      |
| 53 | SRGe J171337.4+581732 | 258.40603  | 58.292136  | 5.0           | 258.404923            | 58.292426             | 2.34                       | 7.7                | 2020-08-18.49      |
| 54 | SRGe J171423.6+085237 | 258.598357 | 8.876814   | 5.0           | 258.598393            | 8.876918              | 0.4                        | 116.83             | 2020-09-18.72      |
| 55 | SRGe J174505.5+104700 | 266.273008 | 10.783297  | 8.69          | 266.272965            | 10.782156             | 4.11                       | 12.16              | 2021-09-24.64      |
| 56 | SRGe J174513.6+401608 | 266.306768 | 40.269026  | 6.77          | 266.308609            | 40.268842             | 5.1                        | 10.18              | 2021-03-22.42      |
| 57 | SRGe J174912.1+595530 | 267.300607 | 59.924895  | 15.13         | 267.302181            | 59.923772             | 4.94                       | 11.03              | 2021-03-16.33      |
| 58 | SRGe J175023.7+712857 | 267.598554 | 71.482499  | 5.0           | 267.599017            | 71.48239              | 0.66                       | 34.34              | 2021-10-07.50      |
| 59 | SRGe J180757.1+565625 | 271.988035 | 56.940306  | 5.19          | 271.987841            | 56.939758             | 2.01                       | 7.61               | 2020-10-10.87      |
| 60 | SRGe J182716.8+044603 | 276.820057 | 4.767595   | 5.61          | 276.819812            | 4.768384              | 2.97                       | 24.94              | 2021-04-05.94      |
| 61 | SRGe J192143.8+503853 | 290.432436 | 50.648059  | 6.78          | 290.432057            | 50.647861             | 1.12                       | 14.65              | 2021-11-06.65      |
| 62 | SRGe J200953.9+672317 | 302.474514 | 67.388044  | 5.79          | 302.47453             | 67.388565             | 1.88                       | 4.76               | 2020-06-28.96      |

**Notes.**  $\alpha_X$ ,  $\delta_X$  are the eROSITA coordinates.  $r_{98}$  is the eROSITA 98% localization region in the stacked eROSITA data ( $r_{98} = 2.8\sigma_{\text{pos}}$ ).  $\alpha_{\text{opt}}$ ,  $\delta_{\text{opt}}$  are the coordinates of optical host galaxy associations.  $\Delta_{\text{pos}}$  ('') represents the angular separation between the X-ray and optical positions of each source.  $f_{X,\text{peak}}$ ,  $t_{X,\text{peak}}$  are the peak X-ray flux ( $10^{-14}$  erg cm $^{-2}$  s $^{-1}$ , 0.3–2.3 keV) from eROSITA multi-epoch observations and the median time of the corresponding epoch with maximum flux.

**Table 2:** Continued table of Tab. 1.

| ID | Name                  | $\alpha_X$ | $\delta_X$ | $r_{98}$ (") | $\alpha_{\text{opt}}$ | $\delta_{\text{opt}}$ | $\Delta_{\text{pos}}$ (") | $f_{X\text{peak}}$ | $t_{X\text{peak}}$ |
|----|-----------------------|------------|------------|--------------|-----------------------|-----------------------|---------------------------|--------------------|--------------------|
| 63 | SRGe J201138.9-210935 | 302.912143 | -21.159756 | 6.26         | 302.912163            | -21.160194            | 1.58                      | 36.89              | 2021-10-29.04      |
| 64 | SRGe J204129.5+214409 | 310.372873 | 21.735758  | 5.0          | 310.372816            | 21.735375             | 1.39                      | 208.1              | 2021-05-11.52      |
| 65 | SRGe J213214.8-003006 | 323.061768 | -0.501774  | 9.49         | 323.062306            | -0.501395             | 2.37                      | 26.09              | 2021-05-14.78      |
| 66 | SRGe J213527.2-181635 | 323.863278 | -18.276355 | 5.0          | 323.86361             | -18.276464            | 1.2                       | 136.41             | 2020-11-09.49      |
| 67 | SRGe J223905.0-270551 | 339.77096  | -27.097538 | 5.0          | 339.769487            | -27.097436            | 4.73                      | 77.17              | 2021-05-18.46      |
| 68 | SRGe J231834.5-351914 | 349.643947 | -35.320561 | 6.4          | 349.645082            | -35.320365            | 3.41                      | 49.11              | 2021-11-22.61      |
| 69 | SRGe J234034.7+293400 | 355.144765 | 29.566581  | 5.0          | 355.144139            | 29.566323             | 2.17                      | 25.02              | 2020-06-17.81      |
| 70 | SRGe J235453.0+421711 | 358.720689 | 42.286526  | 5.0          | 358.720023            | 42.286442             | 1.8                       | 18.83              | 2022-01-04.87      |

SRGe J175023.7+712857 (ID 58) were taken with the 600/4000 grism and a 1" slit. This configuration provided spectral coverage of 3200–10250 Å. For the majority of objects, only one epoch of LRIS spectroscopy was obtained. Multiple spectra were collected for four objects (IDs 5, 26, 58, 66) where prominent TDE emission lines were detected during the first LRIS epoch (see §4.3.4 for details). A log of LRIS observations is presented in Table 3, which also lists the host redshifts measured from the LRIS spectra.

**Table 3:** Keck-I/LRIS spectroscopic observation log.

| ID | Start Date (UT) | Exp. (s) | Redshift       | Phase (d) |
|----|-----------------|----------|----------------|-----------|
| 1  | 2021-10-04.44   | 300      | 0.0727 ±0.0001 | -71       |
| 2  | 2022-07-21.57   | 600      | 0.0535±0.0003  | 400       |
| 3  | 2021-09-07.53   | 600      | 0.1197±0.0002  | -110      |
| 4  | 2023-01-16.26   | 600      | 0.1752±0.0002  | 379       |
| 5  | 2021-08-13.43   | 1800     |                | 40        |
| 5  | 2021-09-07.53   | 900      | 0.1500±0.0001  | 65        |
| 6  | 2022-01-12.18   | 900      | 0.1250±0.0004  | 195       |
| 7  | 2021-07-06.55   | 600      | 0.1314±0.0001  | 363       |
| 8  | 2021-09-07.57   | 300      | 0.0778±0.0001  | 39        |
| 9  | 2022-01-26.27   | 600      | 0.0809±0.0014  | 199       |
| 10 | 2021-08-13.54   | 1485     | 0.3253±0.0001  | 223       |
| 11 | 2021-08-13.54   | 600      | 0.0949±0.0001  | 222       |
| 12 | 2022-07-21.59   | 300      | 0.0338±0.0001  | 719       |
| 13 | 2021-07-06.61   | 750      | 0.3879±0.0001  | 332       |
| 14 | 2022-07-21.60   | 300      | 0.0364±0.0001  | 169       |
| 15 | 2021-08-13.62   | 1480     | 0.2682±0.0005  | 19        |
| 16 | 2022-07-21.61   | 600      | 0.0735±0.0006  | 168       |
| 17 | 2022-07-21.62   | 450      | 0.0180±0.0005  | 339       |
| 18 | 2021-10-04.58   | 300      | 0.0845±0.0001  | 12        |
| 19 | 2021-04-14.26   | 1200     | 0.2221±0.0038  | 15        |
| 20 | 2020-11-20.51   | 900      | 0.1052±0.0001  | 40        |
| 21 | 2021-05-13.27   | 774      | 0.1423±0.0001  | 29        |
| 22 | 2022-02-06.36   | 1160     | 0.2302±0.0003  | 118       |
| 23 | 2021-04-14.30   | 600      | 0.1877±0.0001  | 167       |
| 24 | 2021-05-13.32   | 2508     | 0.4553±0.0004  | 196       |
| 25 | 2021-05-13.26   | 584      | 0.1931±0.0001  | 8         |
| 26 | 2021-07-06.34   | 2709     |                | 29        |
| 26 | 2021-08-13.25   | 1800     | 0.1982±0.0004  | 67        |
| 26 | 2022-02-06.46   | 1770     |                | 244       |
| 27 | 2022-04-07.46   | 1800     | 0.2782±0.0001  | 124       |
| 28 | 2021-06-07.37   | 435      | 0.1491±0.0003  | -10       |
| 29 | 2021-04-14.41   | 400      | 0.1503±0.0001  | 162       |
| 30 | 2022-08-02.28   | 1200     | 0.3091±0.0007  | 614       |
| 31 | 2021-06-07.39   | 285      | 0.0705±0.0002  | 0         |

Continued in next column

| ID | Start Date (UT) | Exp. (s) | Redshift      | Phase (d) |
|----|-----------------|----------|---------------|-----------|
| 32 | 2021-06-07.38   | 435      | 0.1995±0.0004 | 349       |
| 33 | 2021-05-13.36   | 1137     | 0.1889±0.0004 | 132       |
| 34 | 2021-04-14.42   | 300      | 0.1242±0.0003 | -37       |
| 35 | 2021-06-07.41   | 585      | 0.2681±0.0001 | 16        |
| 36 | 2021-05-13.42   | 1756     | 0.3521±0.0006 | 137       |
| 37 | 2021-05-13.43   | 574      | 0.1540±0.0003 | 116       |
| 38 | 2021-06-07.45   | 285      | 0.0679±0.0003 | 314       |
| 39 | 2021-06-07.45   | 285      | 0.1085±0.0002 | 142       |
| 40 | 2022-04-07.54   | 1800     | 0.2437±0.0002 | 113       |
| 41 | 2021-05-13.44   | 574      | 0.2308±0.0004 | 303       |
| 42 | 2021-06-07.47   | 1185     | 0.4385±0.0001 | 150       |
| 43 | 2021-07-06.45   | 600      | 0.1684±0.0003 | -27       |
| 44 | 2021-05-13.46   | 469      | 0.1468±0.0003 | -105      |
| 45 | 2021-04-14.52   | 300      | 0.1304±0.0002 | 242       |
| 46 | 2021-06-07.49   | 580      | 0.1534±0.0003 | -65       |
| 47 | 2022-05-26.40   | 500      | 0.0965±0.0002 | 640       |
| 48 | 2022-05-26.41   | 600      | 0.1415±0.0002 | 97        |
| 49 | 2021-04-14.64   | 500      | 0.2949±0.0009 | 247       |
| 50 | 2021-04-14.54   | 1250     | 0.5813±0.0006 | 253       |
| 51 | 2021-05-13.49   | 254      | 0.2265±0.0007 | 82        |
| 52 | 2022-04-07.56   | 900      | 0.4601±0.0003 | 390       |
| 53 | 2022-02-06.66   | 600      | 0.2624±0.0004 | 537       |
| 54 | 2021-06-07.54   | 280      | 0.0364±0.0001 | 262       |
| 55 | 2025-06-25.39   | 625      | 0.0882±0.0001 | 1370      |
| 56 | 2021-05-13.55   | 1354     | 0.7140±0.0002 | 52        |
| 57 | 2021-05-13.60   | 254      | 0.1089±0.0003 | 58        |
| 58 | 2022-04-07.56   | 900      |               | 182       |
| 58 | 2025-06-01.55   | 975      | 0.0904±0.0002 | 1333      |
| 59 | 2022-07-21.44   | 300      | 0.0602±0.0002 | 649       |
| 60 | 2022-05-26.46   | 750      | 0.0464±0.0003 | 416       |
| 61 | 2022-04-07.60   | 900      | 0.2593±0.0003 | 152       |
| 62 | 2022-07-21.47   | 600      | 0.1203±0.0003 | 753       |
| 63 | 2025-06-01.61   | 1200     | 0.0804±0.0001 | 1312      |
| 64 | 2021-07-06.53   | 600      | 0.1103±0.0003 | 56        |
| 65 | 2022-05-26.57   | 600      | 0.1415±0.0004 | 377       |
| 66 | 2020-11-20.22   | 1140     |               | 11        |
| 66 | 2020-12-12.21   | 600      | 0.0939±0.0001 | 33        |
| 66 | 2021-09-07.43   | 600      |               | 302       |
| 67 | 2021-10-04.43   | 450      | 0.2195±0.0004 | 139       |
| 68 | 2022-07-21.49   | 600      | 0.0549±0.0001 | 241       |
| 69 | 2022-01-12.14   | 600      | 0.1272±0.0003 | 573       |
| 70 | 2022-07-21.05   | 1760     | 0.1990±0.0001 | 197       |

**Notes.** Phase is observer-frame days since eROSITA X-ray peak (i.e.,  $t_{X\text{peak}}$  in Tables 1 and 2). Redshifts are fitted with pPXF from the Keck/LRIS spectra (see §4.2). For sources with multiple spectra (IDs 5, 26, 58, 66), redshifts are determined from the latest, host-dominated spectra. The fitted redshift uncertainties are statistical errors (scaled by  $\sqrt{\chi^2}$ ).

We also cross-matched our sample with the Dark Energy Spectroscopic Instrument (DESI) survey data release one (DR1; [DESI Collaboration et al. 2025](#)). We found DESI spectra for 13 host galaxies in our sample. For 12 of these, the DESI spectra are

broadly consistent with the Keck/LRIS data, exhibiting similar continuum shapes and line properties. Only the one remaining DESI spectrum is retained for our analysis which has substantially higher S/N than the Keck spectrum. The retained DESI spectrum (3600–9800 Å), corresponding to the host galaxy of SRGe J234034.7+293400 (ID 69), was obtained with a single 982 s exposure on 2021-10-16.12 (485 d after the observed peak X-ray flux) using a 1.5'' fiber.

## 4. Analysis

### 4.1. Host Galaxy SED Fitting

To infer host galaxy properties, we fit the galaxy data using `Prospector` (Johnson et al. 2021a) built on `FSPS` (Conroy & Gunn 2010). We adopt a non-parametric continuity star-formation history (SFH) that captures bursts, quenching, and rejuvenation episodes with flexibility.

Our fits use extinction-corrected host galaxy photometry and optical spectroscopy. When jointly fitting photometry and spectroscopy, we employ `Prospector`'s `PolySpecModel` with spectroscopic calibration, including a free normalization parameter (`spec_norm`) to scale the spectrum to match the photometry. Only SRGe J163831.9+534018 (ID 50) was fit using photometry alone, as the joint photometry+spectroscopy fit did not converge. For objects with multiple LRIS spectra (i.e., IDs 5, 26, 58, 66), we use the latest observation.

The LRIS spectra are typically dominated by host galaxy light, as they were obtained at late epochs when the optical counterparts of most X-ray-selected TDEs had faded. However, in some cases, broad emission lines associated with the transient may still be present. We perform the `Prospector` fitting twice: once with the He II  $\lambda 4686$  and  $H\alpha$  regions masked, and once without masking. We adopt the unmasked fits for our final host galaxy parameter estimates, as the transient emission lines are typically weak at these late epochs and their impact on the stellar continuum and broadband photometry is minimal. In §4.3.4, we use the masked fits to identify and characterize any residual broad-line emission from the optical counterparts by subtracting the host model from the observed spectra.

Posterior distributions are sampled with `Dynesty` (Speagle 2020), and convergence is monitored via the built-in KL divergence test. We used the nested sampler with 500 live points (both `nested_nlive_init` and `nested_nlive_batch` set to 500), random-walk sampling mode, a convergence criterion of 0.01 for `nested_dlogz_init`, and a maximum of  $7.5 \times 10^6$  likelihood calls, keeping the default `dynesty` bounds. All fits were run in parallel using MPI via `MPIPool`. We included a multiplicative spectroscopic jitter term (`spec_jitter`) as a free parameter that scales the spectroscopic uncertainties by a wavelength-independent factor, and we did not include any additional jitter term for the photometric data.

The model parameters and measured galaxy properties are described as follows. We adopt a uniform TopHat prior on redshift, constrained to a narrow range of 0.05 around the spectral fitted redshift which is derived from `pPXF` in §4.2. The galaxy stellar mass ( $M_*$ ) is derived from the surviving fraction of stars formed. Stellar metallicity is parameterized as  $\log(Z_*/Z_\odot)$ . We adopt an empirical mass–metallicity prior from Gallazzi et al. (2005). The SFH is represented by logarithmically spaced age bins (with 0–30 Myr and 30–100 Myr fixed). We use 6 bins for spectra with  $(S/N) < 15$ , and typically 10 bins for higher S/N spectra, chosen as a compromise between flexibility and constraining power given the data quality. We adopt a Student's T

prior on the logSFR ratios between adjacent time bins, and recent activity is summarized by the average SFR over the past 10 and 100 Myr (i.e.,  $SFR_{10}$  and  $SFR_{100}$ ). We report the mass-weighted stellar age, defined as the average lookback time of stars weighted by their formed stellar mass across all SFH bins.

Dust is modeled with the two-component prescription of Charlot & Fall (2000), including diffuse ISM optical depth, a birth-cloud fraction, and a variable slope modifier (Kriek & Conroy 2013). From these, we derive  $A_V$  and  $E(B - V)$  for both diffuse and young-star components. As the `FSPS` nebular emission-line grids may not fully capture the diversity of observed line ratios, we model nebular emission with `FSPS+CLOUDY` and enable line-amplitude marginalization, allowing line strengths to vary independently while keeping the stellar-population parameters primarily constrained by the continuum and photometry (Johnson et al. 2021b). These nebular parameters are treated as free parameters and for galaxies with no detectable emission lines, we disable the nebular emission component altogether. For dust emission, we adopt the model of Draine & Li (2007), with  $U_{\min}$ ,  $\gamma_{\text{dust}}$ , and  $Q_{\text{PAH}}$  treated as free parameters when constrained by IR data, and held fixed otherwise. Possible AGN contamination is modeled with the `CLUMPY` torus templates (Nenkova et al. 2008), with  $f_{\text{AGN}}$  and  $\tau_{\text{AGN}}$  held fixed when unconstrained.

The SED fitting results of our gold and silver TDE sample (to be defined later in §4.3) are shown in Appendix A (Figure A.7 and A.8).

### 4.2. Emission-line Fitting

We fit the stellar continuum and nebular emission lines in our optical spectra using the penalized pixel-fitting code `pPXF` (Cappellari 2023) with the `EMILES` stellar library (Vazdekis et al. 2016). For sources with multiple LRIS spectra (IDs 5, 26, 58, 66), we adopt the most recent, host-dominated spectrum for analysis. Each spectrum is modeled with three components: stellar continuum, narrow Balmer emission lines, and narrow forbidden lines. For objects exhibiting broad Balmer wings, we include an additional broad component.

For emission lines with  $S/N \geq 3$ , we adopt the best-fit fluxes and uncertainties from `pPXF`. For lines with  $S/N < 3$ , we perform 1000 Monte Carlo realizations by perturbing the spectra with noise, and use the resulting flux distributions to estimate robust fluxes and uncertainties.

We also measure the equivalent width (EW) of emission lines. EW is defined as

$$\text{EW} = \int \frac{F_{\lambda, \text{obs}} - F_{\lambda, \text{cont}}}{F_{\lambda, \text{cont}}} d\lambda, \quad (1)$$

measured in Å, where  $F_{\lambda, \text{obs}}$  is the observed spectrum, and  $F_{\lambda, \text{cont}}$  is the continuum level estimated as the median flux in the line-free windows on either side of the emission line. The EW uncertainty is calculated via standard error propagation.

### 4.3. Sample Classification

Although the X-ray flares from some AGN can mimic TDEs and contaminate X-ray-selected TDE samples, our ZTF/ATLAS forced photometry and uniform optical spectra for all host galaxies enable a systematic photometric and spectroscopic assessment of AGN interlopers. Below, we examine the available data to remove AGN contaminations, define a gold sample of events that we are most confident are TDEs, and a silver sample of events for which an AGN origin cannot be completely ruled out.

#### 4.3.1. Identification of TDE Candidates with Optical Flares

We visually inspected the ATLAS and ZTF forced photometry light curves from 2018 March 1 to 2024 March 1 (Figures A.3–A.6 in Appendix A) to identify TDE candidates exhibiting optical flares. We only search for optical flares showing a rise and decline, as opposed to stochastic variability characteristic of AGN.

We detected optical flares in 28 objects (IDs 2, 5, 15, 16, 17, 21, 23, 24, 26, 27, 30, 31, 38, 39, 40, 41, 43, 47, 48, 49, 55, 58, 63, 64, 65, 66, 67, 70). Among these, the flares of SRGe J155834.0+382528 (ID 43), SRGe J174505.5+104700 (ID 55) and SRGe J213214.8-003006 (ID 65) exhibit colors ( $g - r \gtrsim 0.5$  mag and  $r - i \gtrsim 0.3$  mag) that are much redder than typical TDEs<sup>2</sup>. The remaining 25 objects display optical flares with colors that are consistent with optically-selected TDEs, with  $g - r < 0.3$  mag at peak.

### 4.3.2. Identification of CrL-TDEs

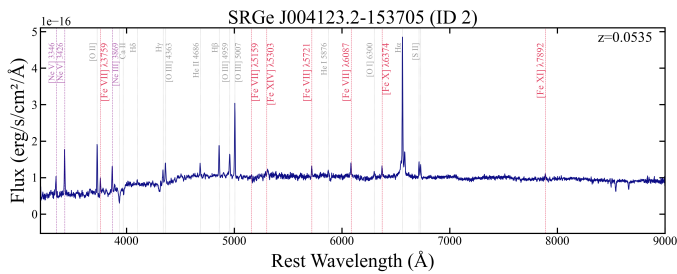


**Fig. 1:** Keck-I/LRIS optical spectrum of SRGe J004123.2-153705 (ID 2), a CrL-TDE.

After examining all LRIS spectra of our candidates, we identified two objects that exhibit high-ionization coronal lines: SRGe J004123.2-153705 (ID 2) and SRGe J201138.9-210935 (ID 63). The optical counterpart of SRGe J201138.9-210935 (ID 63), TDE 2021qth/ZTF21abhrchb, has been previously classified as a CrL-TDE by [Yao et al. \(2023\)](#). The optical counterpart of SRGe J004123.2-153705 (ID 2), AT 2021swi/ZTF21abkqvdo, exhibited an optical flare with a well-defined rise and decline coincident with the X-ray detection (see Figure A.3), along with the characteristic spectroscopic features of a CrL-TDE (Figure 1). We therefore classify it as a CrL-TDE as well.

### 4.3.3. Removal of AGN Interlopers

The AGN population can be broadly divided into BLAGN and narrow-line AGN (NLAGN) based on the full-width at half-maximum (FWHM) of H $\alpha$ , with BLAGN exhibiting FWHM > 10<sup>3</sup> km s<sup>-1</sup> (Stern & Laor 2012). In the AGN unification model (Antonucci 1993), BLAGN are viewed at low inclinations where high-energy X-ray emission from the central engine is directly observable, while NLAGN are viewed at higher inclinations where X-rays are obscured by the dusty torus. We conservatively exclude all BLAGN from our sample, as intrinsic variations in the accretion rate can produce substantial X-ray flux changes that mimic TDE flares. For NLAGN, however, we assess whether the observed X-ray flare luminosity is consistent with typical AGN variability. We retain NLAGN as TDE candidates only if the X-ray flare significantly exceeds the luminosity

<sup>2</sup> In §4.3.3, we show that optical spectra obtained long after the flare faded exhibit typical AGN signatures.

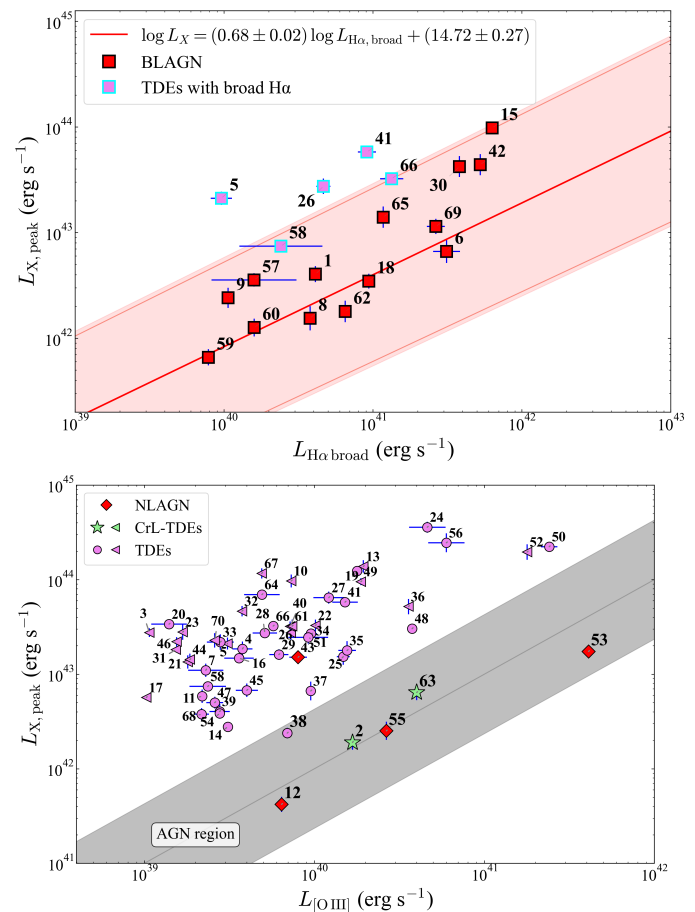


**Fig. 2:** Top: Peak 0.3–2.3 keV X-ray luminosity versus broad H $\alpha$  luminosity. The solid line shows the best-fit relation from the corrected calibration of [Pulatova et al. \(2025\)](#), and the shaded region indicates the intrinsic scatter of the correlation. Note that the H $\alpha$  luminosity of SRGe J234034.7+293400 (ID 69), is derived from DESI spectrum (see §3.2), while others are all from Keck LRIS spectra. Bottom:  $L_{\text{X,peak}}$  versus [O III] $\lambda 5007$  luminosity for the remaining sources. The shaded region shows the AGN locus ([Ueda et al. 2015](#)) calibrated in the eROSITA 0.3–2.3 keV band ([Khorunzhev et al. 2022](#)), with the solid line indicating the median relation  $\log(L_{\text{[O III]}}/L_{\text{X}}) = -1.99 \pm 0.63$ . Left-pointing triangles denote sources with upper limits on [O III] line luminosity.

expected from AGN activity, indicating a distinct transient event rather than normal AGN variability.

We identify BLAGN by requiring a broad H $\alpha$  component with FWHM > 1000 km s $^{-1}$  in the pPXF fitting results (§4.2). pPXF detects 20 sources with broad H $\alpha$  emission<sup>3</sup>. The top panel of Figure 2 shows the distribution of these sources in the peak X-ray luminosity versus broad H $\alpha$  line luminosity plane. We use the empirical  $L_X$ – $L_{\text{H}\alpha, \text{broad}}$  relation from [Pulatova et al. \(2025\)](#) as the primary diagnostic for identifying BLAGN. A total of 13 objects (IDs 1, 6, 8, 9, 18, 30, 42, 57, 59, 60, 62, 65, 69) fall within the BLAGN locus and are classified accordingly. Two of these (IDs 30 and 65) exhibit optical flares identified in §4.3.1. The optical flare of ID 65 has AGN-like colors, while the colors of ID 30 are poorly constrained. We conservatively classify both as likely BLAGN flares rather than TDEs.

Three sources (IDs 15, 58, 66) fall near the upper edge of the BLAGN locus and require additional scrutiny. SRGe J023440.1-

<sup>3</sup> For sources with multiple spectra, we use the spectrum obtained closest to the X-ray peak to compute H $\alpha$  line luminosities.

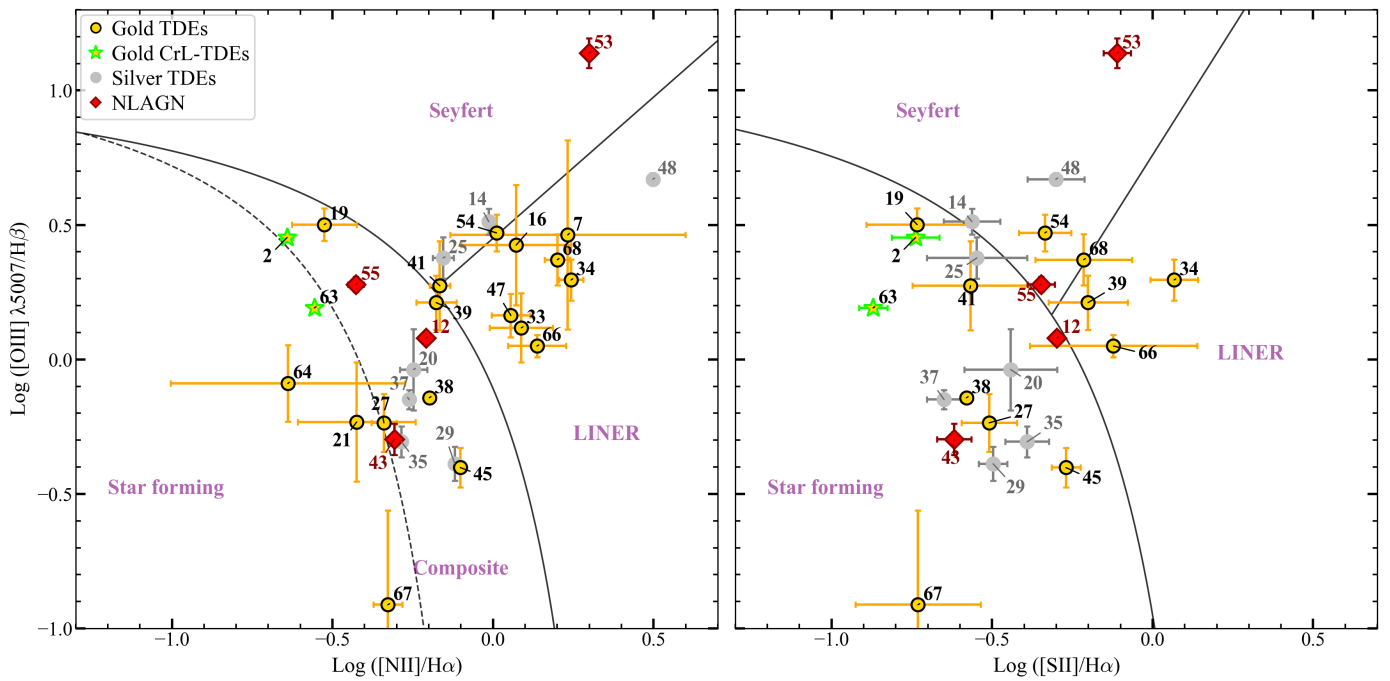


**Fig. 3:** BPT diagrams of host galaxies. The solid curves mark the theoretical maximum starburst demarcations of Kewley et al. (2006), and the dashed curve in the left panel shows the empirical star-forming/composite boundary from Kauffmann et al. (2003a).

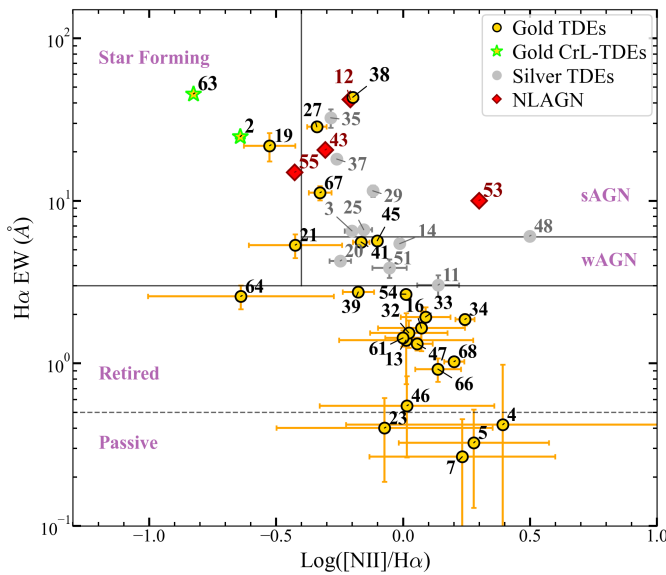


**Fig. 4:** WHAN diagram of host galaxies. The horizontal lines at  $\text{EW}(\text{H}\alpha) = 6 \text{ \AA}$  and  $3 \text{ \AA}$  indicate the sAGN/wAGN and wAGN/retired divisions, respectively, following Cid Fernandes et al. (2011).

021812 (ID 15) exhibits, in addition to broad Balmer lines, broad  $\text{H}\beta$  and broad  $\text{Mg II } \lambda\lambda 2796, 2803$  emission which is rarely detected in known TDEs (Hung et al. 2019), favoring a BLAGN interpretation. In contrast, SRGe J175023.7+712857 (ID 58) and SRGe J213527.2-181635 (ID 66) both display broad helium lines (see §4.3.4) characteristic of TDEs and are therefore classified as TDEs with broad  $\text{H}\alpha$  rather than BLAGN.

The remaining three sources with detected broad  $\text{H}\alpha$  (IDs 5, 26, 41) all exhibit TDE-like optical flares (§4.3.1). For IDs 5 and 26, LRIS spectra obtained during the optical flares show transient broad  $\text{He II}$  features (see §4.3.4), indicating the broad lines

are transient rather than AGN-driven. For ID 41, LRIS spectra were obtained after the optical flares faded below ZTF sensitivity. Given the absence of other typical BLAGN signatures (broad  $\text{H}\beta$ , stochastic variability, or broad  $\text{Mg II}$ ), we interpret the detected broad  $\text{H}\alpha$  as associated with the TDE optical flare.

Some of the X-ray transients are likely powered by NLAGN. To identify this population, we analyze the relation between the  $[\text{O III}] \lambda 5007$  line luminosity ( $L_{[\text{O III}]}$ ) and the peak X-ray luminosity, along with the Baldwin, Phillips & Terlevich (BPT; Baldwin et al. 1981) and WHAN (Cid Fernandes et al. 2011) diagnostic diagrams.

The BPT diagram classifies galaxies using flux ratios of emission lines that are close in wavelengths. This diagnostic framework distinguishes four galaxy types: star-forming, composite, Seyfert, and Low-Ionization Nuclear Emission-line Region (LINER; Heckman 1980) galaxies. Seyfert galaxies are AGN dominated by accretion-powered nuclear emission. Composite galaxies occupy an intermediate region and show mixed contributions from both star formation and AGN ionization (Kewley et al. 2006). The ionization source in LINER galaxies remains debated: while many LINERs harbor low-luminosity AGN, alternative mechanisms including shocks, outflows, or photoionization by post-asymptotic giant branch (post-AGB) stellar populations may also contribute (Ho et al. 1993; Filippenko 1996; Singh et al. 2013).

We employ two BPT diagrams using  $[\text{O III}]/\text{H}\beta$  versus  $[\text{N II}]/\text{H}\alpha$  and  $[\text{S II}]/\text{H}\alpha$  ratios (Figure 3). Not all gold and silver sources appear in these diagrams, as BPT classification requires reliable measurements of  $[\text{O III}]$ ,  $[\text{N II}]$ ,  $[\text{S II}]$ , narrow  $\text{H}\beta$  and narrow  $\text{H}\alpha$ . We only plot sources for which all required lines are detected with  $\text{S/N} \geq 5$ . The two BPT panels are generally consistent with each other, with no sources appearing as star-forming on one panel while being classified as Seyfert or LINER on the other. Discrepancies mainly occur among sources classified as Composite, Seyfert, or LINER. For sources that fall into different regions among these three categories between the

two BPT panels, we conservatively adopt the classification indicating AGN presence (Seyfert or LINER) in BPT diagnostic to ensure robust AGN exclusion from our gold TDE sample (see §4.3.5).

Many systems classified as composite or LINER on the BPT diagram are not genuine AGN. The WHAN diagram provides a cleaner separation between true AGN and such contaminants using the EW of  $H\alpha$  and the  $[N\,II]/H\alpha$  line flux ratio (Cid Fernandes et al. 2011). This framework classifies galaxies into five categories: star forming, strong AGN (sAGN), weak AGN (wAGN), retired, and passive. As with BPT, WHAN classification requires reliable narrow  $H\alpha$  and  $[N\,II]$  measurements, so sources lacking these measurements are not shown (Figure 4). Galaxies classified as LINER in the BPT diagram but falling outside the sAGN or wAGN regions in the WHAN diagram are more consistent with ionization by hot evolved stars (e.g., post-AGB stars) rather than accretion activity. Similarly, BPT-composite galaxies falling outside the WHAN-sAGN region are more consistent with ionization by diffuse gas or evolved stellar populations rather than an active nucleus.

On the  $L_{[OIII]}-L_X$  diagram (bottom panel of Figure 2), four sources that are not classified as CrL-TDEs fall within the AGN locus (IDs 12, 38, 53, and 55). Three (IDs 12, 53, 55) are independently confirmed as AGN by both BPT and WHAN diagnostics (Figures 3 and 4) and are classified as NLAGN. The remaining source, SRGe J153134.9+330539 (ID 38; AT 2020ocn/ZTF20aabqihu), shows evidence for a TDE origin: it was previously identified as a TDE-He by Hammerstein et al. (2023) and exhibits strong early-time X-ray variability (Cao et al. 2024).

Finally, we consider SRGe J155834.0+382528 (ID 43), which exhibits a red optical flare (§4.3.1; Figure A.5). Although it does not fall within the AGN locus in Figure 2, it is classified as star-forming/composite in the BPT diagram and as sAGN in the WHAN diagram. We therefore conservatively classify it as an AGN flare rather than a TDE.

In summary, we identify 18 objects as AGN interlopers (IDs 1, 6, 8, 9, 12, 15, 18, 30, 42, 43, 53, 55, 57, 59, 60, 62, 65, 69).

#### 4.3.4. Identification and Modeling of Broad TDE Lines in LRIS Spectra

In this section, we examine whether broad emission lines associated with the optical TDEs are detected in the LRIS spectra. We focus on the 50 objects that are not classified as AGN interlopers (§4.3.3) or CrL-TDEs (§4.3.2). As noted above, four TDEs (IDs 5, 26, 58, 66) have multiple LRIS observations in which prominent broad lines that are well above the continuum and easily identifiable by eye are detected in earlier epochs.

Do we expect to detect broad lines in the remaining 46 candidates? In most cases, the LRIS follow-up occurred sufficiently late that the optical flare had faded below the ZTF sensitivity limit. According to the forced-photometry light curves in Appendix A, only three objects (IDs 17, 24, 49) were observed while the optical flare was still detectable by ZTF. ID 17 was previously classified as a featureless TDE based on early-time observations (Yao et al. 2022), while IDs 24 and 49 have faint continuum fluxes ( $f_v \lesssim 3 \mu\text{Jy}$ ,  $m \gtrsim 22.7$  mag) such that transient emission might be dominated by host-galaxy light. Nevertheless, broad lines could remain visible in our spectra even when ZTF forced photometry shows no optical flare, provided their luminosities fall below the ZTF detection threshold.

To systematically search for broad lines around the  $He\,II$  and  $H\alpha$  regions in the 46 candidates, we use the two `Prospector` fits

described in §4.1. We first inspect the `Prospector` fits in which the  $He\,II$  and  $H\alpha$  regions are masked. We require the significance of EW of the  $He\,II$  (4000–5300 Å) or  $H\alpha$  (6400–6800 Å) regions to be greater than five. This procedure yields four candidates exhibiting broad-line excess (IDs 39, 41, 64, 70). Because template mismatch can produce spurious residuals, we also examine the unmasked `Prospector` fits. The broad-line excess persists in IDs 39, 41, and 70 but disappears for ID 64.

In total, we therefore identify seven objects with flux excess around common TDE broad line regions in LRIS spectroscopy (IDs 5, 26, 39, 41, 58, 66, 70). Following Charalampopoulos et al. (2022), we measure their line fluxes after subtracting two components from the observed LRIS spectra: (1) a scaled `Prospector` stellar continuum model (with  $He\,II$  and  $H\alpha$  masked) representing the host contribution, and (2) a low-order polynomial accounting for the optical flare continuum. In Figure 5, the black lines in the top panels show the observed spectra ( $F_{\lambda,\text{obs}}$ ), and the red lines show the combined continuum model ( $F_{\lambda,\text{cont}}$ ).

We model the emission lines with Gaussian profiles to determine their fluxes and kinematics. In the  $H\alpha$  region (6400–6700 Å), the main components include a narrow and a broad  $H\alpha$  component, and the  $[N\,II]$   $\lambda\lambda 6548, 6583$  doublet whose flux ratio is fixed at the theoretical value of 1:3. We include additional free-centered Gaussian components as needed to capture complex line structure (Nicholl et al. 2019; Charalampopoulos et al. 2022; Kumar et al. 2024)<sup>4</sup>. In the  $He\,II$  region (4000–5300 Å), we simultaneously fit  $He\,II$   $\lambda 4686$ ,  $H\beta$ , and Bowen blend features using both broad and narrow Gaussian components. For SRGe J235453.0+421711 (ID 70), which exhibits asymmetric blueshifted  $He\,II$  emission, we employ skewed Gaussian profiles following Kumar et al. (2024).

Model selection is guided by the Bayesian Information Criterion (BIC). A more complex model is adopted only when the improvement exceeds  $\Delta\text{BIC} > 10$ , a threshold commonly interpreted as very strong evidence in favor of the more complex model (Kass & Raftery 1995; Lorah & Womack 2019). This criterion ensures that additional components are statistically justified while minimizing the risk of overfitting. The measured line properties (luminosity, FWHM, EW) are presented in Table B.1 of Appendix B. We note that broad line detections in SRGe J153331.5+390536 (ID 39) have rather low significance ( $5.2\sigma$  for  $He\,II$  and  $2.0\sigma$  for  $H\alpha$ ), and we therefore exclude this object from further discussion. The residual spectra and Gaussian fitting results for the other six objects are shown in the bottom panels of Figure 5.

For spectra where  $H\alpha$  or  $He\,II$   $\lambda 4686$  lines are not detected, we computed  $3\sigma$  upper limits on line luminosities from the residual spectrum. We integrate the residual flux over  $\pm 500 \text{ km s}^{-1}$  velocity windows centered on each line. To properly account for measurement uncertainties, we performed 10,000 Monte Carlo realizations by perturbing the spectra with noise. The 99.73rd percentile of the resulting flux distribution defines the  $3\sigma$  upper limit. These luminosity upper limits are also listed in Table B.1 (Appendix B). We discuss the results of this analysis in §5.2.

#### 4.3.5. Final Sample Definition

Among the 70 eROSITA TDE candidates, we identified 18 AGN interlopers in §4.3.3. To further identify high-confidence TDEs

<sup>4</sup> While multiple (3–4) Gaussians do not constitute a physical model, this approach provides a simple mathematical framework for characterizing features with complex morphologies.

**Table 4:** The gold TDE sample.

| ID | Name                  | Type in BPT     | Type in WHAN    | Optical flare | Spectral subtype | Reference             | IAU name    | ZTF name     |
|----|-----------------------|-----------------|-----------------|---------------|------------------|-----------------------|-------------|--------------|
| 2  | SRGe J004123.2-153705 | SF              | SF              | ✓             | Cl-L-TDE         |                       | AT 2021swi  | ZTF21abkqvdo |
| 4  | SRGe J010445.8+044319 | —               | Retired/Passive | ✗             | —                |                       |             |              |
| 5  | SRGe J011603.1+072258 | —               | Passive         | ✓             | TDE-H+He         |                       |             |              |
| 7  | SRGe J013204.4+122235 | LINER/Seyfert   | Passive         | ✗             | —                | Sazonov et al. (2021) |             |              |
| 10 | SRGe J015754.6-154214 | —               | —               | ✗             | —                | Sazonov et al. (2021) |             |              |
| 13 | SRGe J021939.7+361819 | —               | Retired         | ✗             | —                | Sazonov et al. (2021) |             |              |
| 16 | SRGe J025548.1+142800 | LINER/Seyfert   | Retired         | ✓             | —                |                       |             |              |
| 17 | SRGe J030747.8+401842 | —               | —               | ✓             | TDE-featureless  |                       |             |              |
| 19 | SRGe J060324.7+621112 | Composite       | SF              | ✗             | —                | Yao et al. (2022)     | TDE 2021ehb | ZTF21aanxhjv |
| 20 | SRGe J071310.4+725627 | Composite       | wAGN            | ✓             | —                | Sazonov et al. (2021) |             |              |
| 21 | SRGe J081006.4+681755 | SF/Composite    | SF/wAGN         | ✓             | —                |                       |             |              |
| 22 | SRGe J083640.9+805410 | —               | —               | ✗             | —                | Sazonov et al. (2021) |             |              |
| 23 | SRGe J091747.3+524818 | —               | Retired/Passive | ✓             | —                | Sazonov et al. (2021) |             |              |
| 24 | SRGe J095928.7+643024 | —               | —               | ✓             | —                | Sazonov et al. (2021) |             |              |
| 26 | SRGe J131014.7+444319 | —               | —               | ✓             | TDE-H+He         |                       |             |              |
| 27 | SRGe J131404.1+515427 | SF/Composite    | sAGN            | ✓             | —                |                       |             |              |
| 28 | SRGe J132718.1+350437 | —               | —               | ✓             | —                |                       |             |              |
| 31 | SRGe J135353.7+535949 | —               | —               | ✓             | TDE-He           |                       |             |              |
| 32 | SRGe J135515.0+311605 | —               | Retired         | ✗             | —                |                       |             |              |
| 33 | SRGe J135812.1+195357 | LINER           | Retired         | ✗             | —                |                       |             |              |
| 34 | SRGe J144738.3+671818 | LINER           | Retired         | ✗             | —                |                       |             |              |
| 38 | SRGe J153134.9+330539 | Composite       | sAGN            | ✓             | TDE-H+He         |                       |             |              |
| 39 | SRGe J153331.5+390536 | Comp/Sey/LIN    | Retired         | ✓             | —                |                       |             |              |
| 40 | SRGe J153403.5+621851 | —               | —               | ✓             | TDE-H?           |                       |             |              |
| 41 | SRGe J153503.3+455054 | Comp/Sey/LIN    | wAGN            | ✓             | —                |                       |             |              |
| 44 | SRGe J160943.1+253603 | —               | —               | ✗             | —                |                       |             |              |
| 45 | SRGe J161001.3+330120 | Composite       | wAGN            | ✗             | —                |                       |             |              |
| 46 | SRGe J161559.1+360156 | —               | Retired/Passive | ✗             | —                |                       |             |              |
| 47 | SRGe J162159.4+271133 | LINER           | sAGN/wAGN       | ✓             | —                |                       |             |              |
| 48 | SRGe J162932.1+280521 | LINER/Seyfert   | —               | ✓             | TDE-H+He         |                       |             |              |
| 49 | SRGe J163030.3+470125 | —               | —               | ✗             | —                |                       |             |              |
| 50 | SRGe J163831.9+534018 | —               | Retired         | ✗             | —                |                       |             |              |
| 54 | SRGe J171423.6+085237 | LINER/Seyfert   | —               | ✓             | —                |                       |             |              |
| 58 | SRGe J175023.7+712857 | —               | Retired         | ✗             | Cl-L-TDE         |                       |             |              |
| 61 | SRGe J192143.8+503853 | SF              | Retired         | ✓             | —                |                       |             |              |
| 63 | SRGe J201138.9-210935 | SF/Composite    | SF              | ✓             | —                |                       |             |              |
| 64 | SRGe J204129.5+214409 | Composite/LINER | Retired         | ✓             | TDE-H+He         |                       |             |              |
| 66 | SRGe J213527.2-181635 | SF              | Retired         | ✓             | —                |                       |             |              |
| 67 | SRGe J223905.0-270551 | SF              | sAGN            | ✓             | —                |                       |             |              |
| 68 | SRGe J231834.5-351914 | LINER/Seyfert   | Retired         | ✗             | TDE-He           |                       |             |              |
| 70 | SRGe J235453.0+421711 | —               | —               | ✓             | —                |                       |             |              |

**Notes.** In the “Spectral subtype” column, we list subtype classifications only if available from the literature or if we detect coronal lines or broad emission lines associated with the TDE in this work.

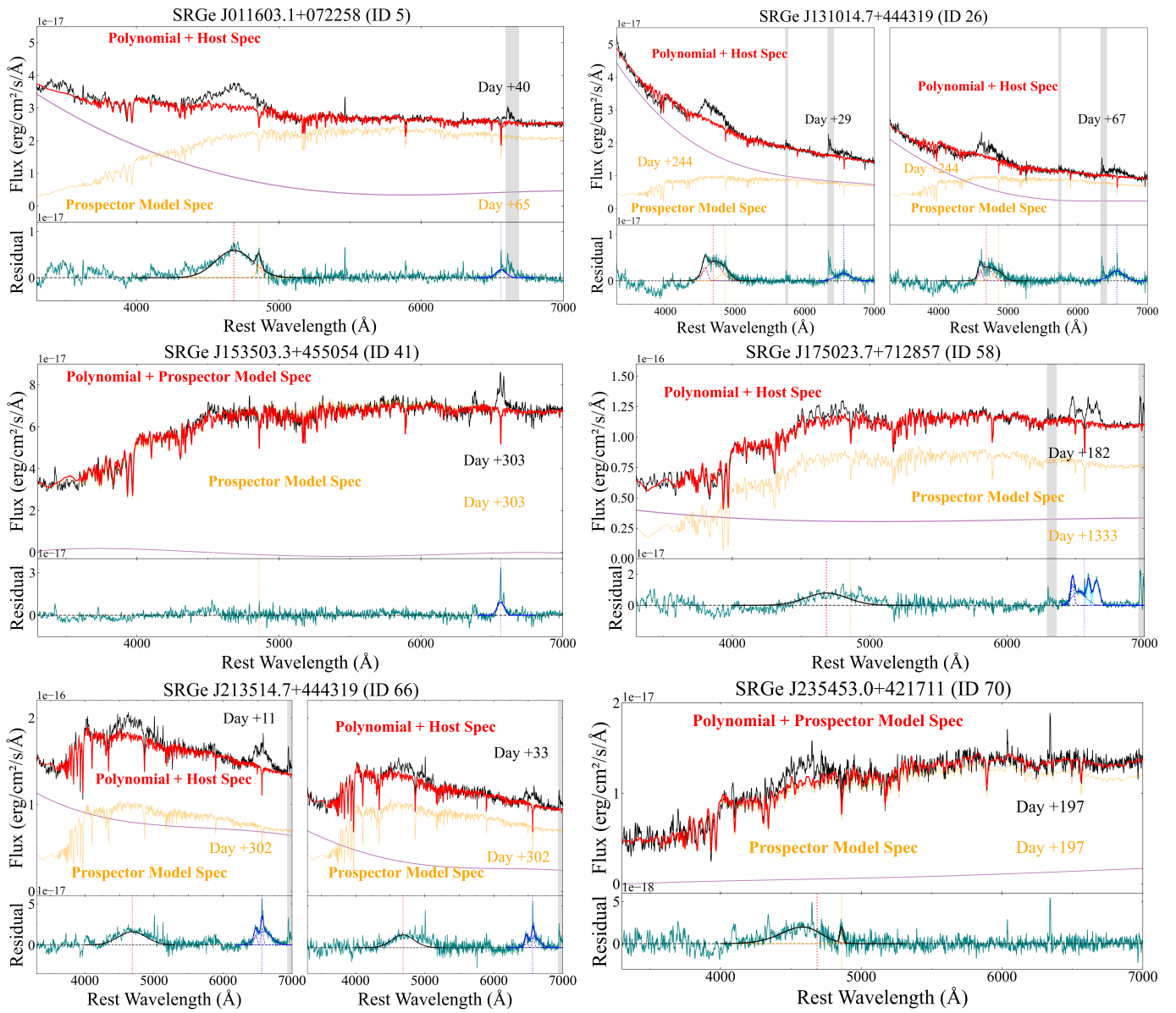


**Fig. 5:** Spectral modeling of six objects with broad lines associated with the TDE. The observed LRIS data is shown in black. The orange line shows the Prospector-derived host model, and the red line shows the final continuum (polynomial fit plus scaled host model). The continuum-subtracted residuals are shown in teal. The individual Gaussian fits are shown as dashed curves, with vertical dotted lines marking their rest-frame wavelengths: purple for the Bowen blend, red for  $\text{He II } \lambda 4686$ , orange for  $\text{H}\beta$ , and blue for the broad component of  $\text{H}\alpha \lambda 6563$ . The solid black and blue curves show the total models in the  $\text{He II}$  and  $\text{H}\alpha$  regions, respectively. Grey bands indicate masked telluric regions.

among the remaining 52 objects, we define a gold sample using the following criteria:

1. Events with TDE-like optical flares (§4.3.1) that are not classified as AGN interlopers (§4.3.3) are included in the gold sample. A total of 23 events satisfy this criterion (IDs 2, 5, 16, 17, 21, 23, 24, 26, 27, 31, 38, 39, 40, 41, 47, 48, 49, 58, 63, 64, 66, 67, 70).
2. For the remaining 29 events, those with host galaxies classified as retired or passive on the WHAN diagram are included. A total of 10 events satisfy this criterion (IDs 4, 7, 13, 32, 33, 34, 46, 54, 61, 68).
3. For the remaining 19 events, those with host galaxies classified as composite on the BPT diagram and non-sAGN on the WHAN diagram are included. A total of 3 events satisfy this criterion (IDs 19, 20, 45).

4. Among the remaining 16 events, 8 lack detected emission lines and therefore do not appear in the BPT and WHAN diagrams (IDs 10, 22, 28, 36, 44, 50, 52, 56). Five of these (IDs 10, 22, 28, 44, 50) are quiescent galaxies with minimal emission, while three (IDs 36, 52, 56) have low signal-to-noise spectra near the  $\text{H}\alpha$  and/or  $\text{H}\beta$  regions. We include the five quiescent galaxy hosts in the gold sample, as they show no AGN signatures.

Our final classification yields a gold sample of 41 objects (Table 4) and a silver sample of 11 objects (Table 5).

#### 4.4. SDSS Comparison Sample

We construct a volume-limited SDSS comparison sample for TDE host galaxies based on completeness. First, we identify the

**Table 5:** The silver TDE sample.

| ID | Name                  | Type in BPT  | Type in WHAN |
|----|-----------------------|--------------|--------------|
| 3  | SRGe J010301.0-130120 | —            | sAGN/wAGN    |
| 11 | SRGe J015907.1-150323 | —            | wAGN/Retired |
| 14 | SRGe J023017.3+283606 | Comp/Seyfert | WAGN         |
| 25 | SRGe J113323.2+693635 | Comp/Sey/LIN | sAGN         |
| 29 | SRGe J133053.5+734823 | Composite    | sAGN         |
| 35 | SRGe J145226.6+670437 | Composite    | sAGN         |
| 36 | SRGe J150328.1+495117 | —            | —            |
| 37 | SRGe J152656.3+353317 | Composite    | sAGN         |
| 51 | SRGe J165055.8+301634 | —            | wAGN         |
| 52 | SRGe J170139.0-085911 | —            | —            |
| 56 | SRGe J174513.6+401608 | —            | —            |

**Notes.** SRGe J023017.3+283606 (ID 14) has been identified as an X-ray transient with monthly quasi-periodic eruptions (Evans et al. 2023; Guolo et al. 2024b). SRGe J133053.5+734823 (ID 29) was reported as a possible TDE by Sazonov et al. (2021), but it does not pass our classification scheme as it is classified as composite in the BPT diagram and sAGN in the WHAN diagram, so we retain it only in the silver sample.

minimum stellar mass in our TDE sample ( $M_{*,\min} = 10^{9.3} M_{\odot}$ ), then compute the completeness redshift  $z_{\text{complete}}$  by analyzing the number density  $\phi(z)$  of SDSS galaxies in a mass bin ( $\pm 0.15$  dex) centered on  $M_{*,\min}$ . The number density is calculated in redshift bins of  $\Delta z = 0.01$ , accounting for comoving volume effects.  $z_{\text{complete}}$  is defined as the redshift where the density drops below 70% of its reference value, computed over  $z = 0.02$ –0.06, yielding  $z_{\text{complete}} = 0.065$ .

We select SDSS galaxies with  $z < z_{\text{complete}} = 0.065$ . The sample is cross-matched with the stellar mass catalog from Mendel et al. (2014) and the NYU Value-Added Galaxy Catalog (Blanton et al. 2005), and rest-frame  $u - r$  colors are computed from K-corrected photometry. This results in a volume-limited sample of 144,801 SDSS galaxies. For spectral feature analysis, we further require SDSS galaxies to have measurements in the MPA-JHU catalog (Kauffmann et al. 2003b; Brinchmann et al. 2004; Tremonti et al. 2004).

## 5. Results and Discussion

### 5.1. Optical Light Curves of X-ray selected TDEs

Here we discuss the optical light curve properties of X-ray-selected TDEs. In our gold TDE sample, 23 of 41 events exhibit optical flares detected in forced photometry. Peak optical luminosities ( $L_{\text{opt,peak}}$ ) are computed using the best-fit Gaussian process models shown in Appendix A (Figures A.3–A.6). For events without detected optical flares, we report  $3\sigma$  upper limits, where  $\sigma$  is the greater of either the median forced photometry flux uncertainty or the standard deviation of the forced photometry flux<sup>5</sup>.

Figure 6 shows the distribution of our gold sample in the  $L_{\text{opt,peak}}$  versus  $L_{\text{X,peak}}$  plane. Note that peak X-ray luminosity  $L_{\text{X,peak}}$  is estimated from the observed peak flux ( $f_{\text{X,peak}}$  in Tables 1 and 2) captured by the 6-month-cadence eROSITA survey

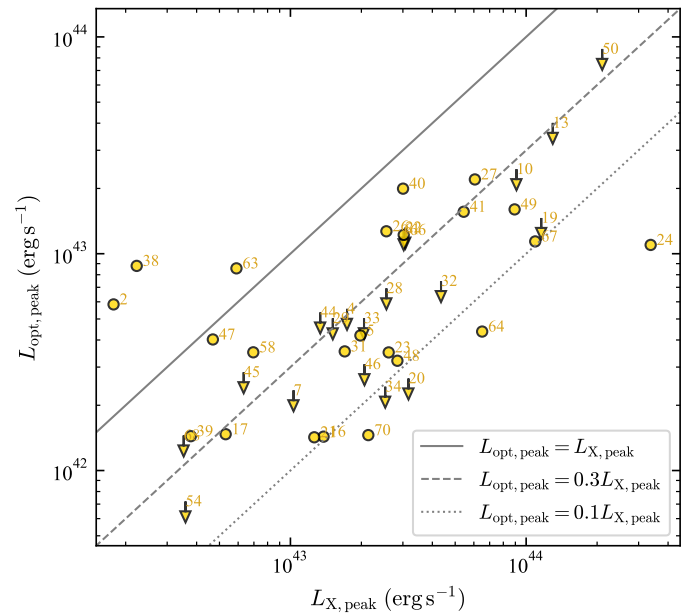


**Fig. 6:** Peak optical luminosity versus peak X-ray luminosity for the 43 TDEs in our gold sample.

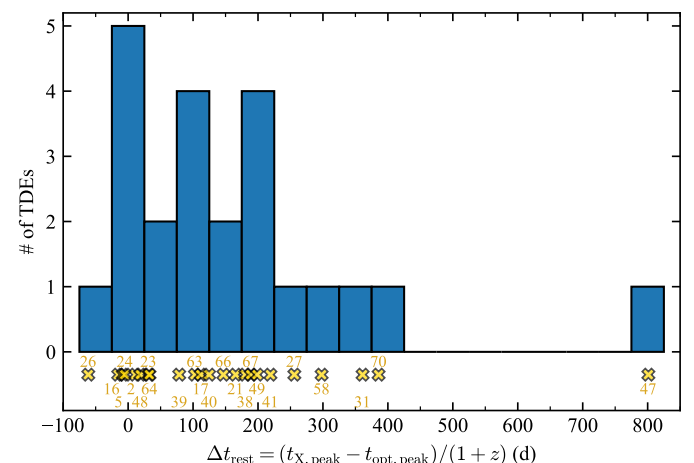


**Fig. 7:** Time difference between the peak X-ray and peak optical emission. The distribution is shown as a histogram, with individual measurements marked along the x-axis. Our sample demonstrates that delayed X-ray peak is common among X-ray selected TDEs.

and is therefore likely fainter than the true intrinsic X-ray peak. Nevertheless, 38 of 41 events have  $L_{\text{opt,peak}} < L_{\text{X,peak}}$ , demonstrating that the vast majority of X-ray-selected TDEs are intrinsically brighter in X-rays than in the optical.

Delayed X-ray brightening is commonly observed in optically selected TDEs (Guolo et al. 2024a). This raises the question of whether this feature is intrinsic to the TDE population or a result of selection effects. To investigate this, we measure the time difference between the time of the peak X-ray flux detected by eROSITA ( $t_{\text{X,peak}}$  in Tables 1 and 2) and the optical peak from the best-fit Gaussian process models (Appendix A; Figures A.3–A.6). This estimate has large uncertainties for individual events due to eROSITA’s 6-month cadence and seasonal gaps in optical light curves. However, with 23 events exhibiting optical flares, the distribution of rest-frame time difference

<sup>5</sup> Note that in our previous work (Sazonov et al. 2021), we considered only the median forced photometry flux uncertainty. However, forced photometry uncertainties can be underestimated; the standard deviation provides a more conservative estimate.

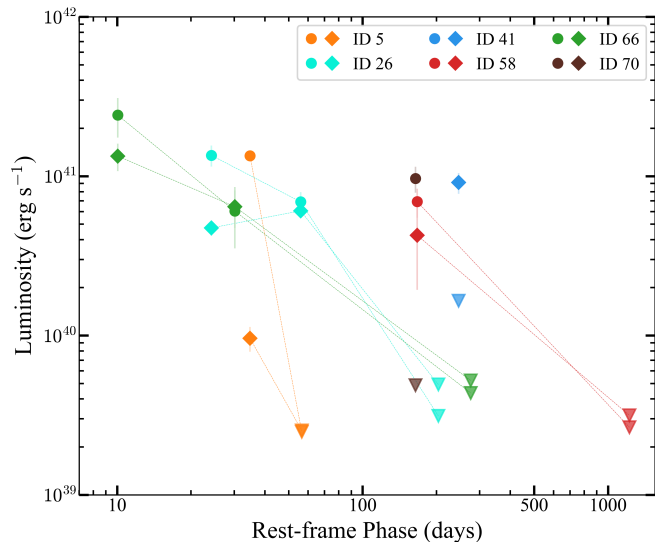
$[\Delta t_{\text{rest}} = (t_{\text{X,peak}} - t_{\text{opt,peak}})/(1+z)]$  provides meaningful constraints on the underlying population properties.

Figure 7 shows the distribution of  $\Delta t_{\text{rest}}$ , which is positively skewed (skewness = 1.85). The median time difference is 125 days, with 68% of events falling between 3 d and 276 d (16th and 84th percentiles, respectively). The 90% range spans –15 d to 383 d. Despite the large uncertainties in the peak time estimates, a number of events exhibit  $\Delta t_{\text{rest}}$  values that are consistent with zero, indicating nearly simultaneous X-ray and optical peaks. We note that delayed X-ray brightening, while common, exhibits substantial event-to-event variation.

We highlight two events. SRGe J131014.7+444319 (ID 26) has the smallest value of  $\Delta t_{\text{rest}} = -61$  d, with the eROSITA detection occurring near the beginning of the optical flare (Figure A.4). This event may be analogous to TDE 2022dsb, which showed transient fading X-ray emission detected by eROSITA-DE during the rise of the optical light curve (Malyali et al. 2024). At the opposite extreme, SRGe J162159.4+271133 (ID 47) exhibits the longest delay,  $\Delta t_{\text{rest}} = 801$  d (see Figure A.5). However, without prompt X-ray follow-up observations, we cannot constrain the physical origin of the X-ray emission in either case.

## 5.2. Optical Broad-line Properties of X-ray selected TDEs

In §4.3.4, we identified significant broad emission lines around He II  $\lambda 4686$  and  $\text{H}\alpha$  in LRIS spectra of six objects. Figure 8 displays the evolution of their line luminosities. Below, we discuss their possible physical origins.



**Fig. 8:** Broad emission line luminosity evolution for six TDEs with significant broad lines detected in our Keck spectra (see §4.3.4). Circles and diamonds represent the fitted luminosity of He II  $\lambda 4686$  (broad or shifted components) and  $\text{H}\alpha$  (broad + shifted components) transient lines, respectively. Downward triangles indicate  $3\sigma$  upper limits.

### 5.2.1. Broad $\text{H}\alpha$ without He (ID 41)

SRGe J153503.3+455054 (ID 41) exhibits intermediate-width (FWHM  $\sim 2700$  km s $^{-1}$ ) luminous ( $\sim 10^{41}$  erg s $^{-1}$ )  $\text{H}\alpha$  emission  $\sim 300$  d after the X-ray peak ( $\sim 500$  d after the optical peak). The line width and luminosity are reminiscent of features reported by Somalwar et al. (2025), which may originate from dense clumps of outflowing gas in the circumnuclear medium.

### 5.2.2. Broad He without $\text{H}\alpha$ (ID 70)

SRGe J235453.0+421711 (ID 70) exhibits an asymmetric broad feature consistent with luminous ( $\sim 10^{41}$  erg s $^{-1}$ ) He II  $\lambda 4686$  emission that is blueshifted with pronounced negative skewness<sup>6</sup>. The line exhibits FWHM  $\sim 2 \times 10^4$  km s $^{-1}$  and is blueshifted by 0.04c relative to the rest frame, which is comparable to FWHM (0.08c). Similar profiles have been observed in optically selected TDEs such as TDE 2019qiz (Nicholl et al. 2020) and TDE 2023vto (Kumar et al. 2024), consistent with emission from an expanding, optically thick outflow where line broadening is dominated by bulk gas motion.

### 5.2.3. Broad $\text{H}\alpha$ and He (IDs 5, 26, 58, 66)

Four objects (IDs 5, 26, 58, 66) show both He II  $\lambda 4686$  and  $\text{H}\alpha$  broad lines, all with multiple LRIS spectra. A common feature is extremely broad He II  $\lambda 4686$  (FWHM  $\gtrsim 2 \times 10^4$  km s $^{-1}$ ). The best-fit Gaussian centers are consistent with the rest-frame wavelength, indicating that the line broadening is dominated by electron scattering rather than bulk kinematic motion. This suggests that in X-ray-selected TDEs, the He II line photosphere is likely located closer to the central ionizing source, resulting in higher electron scattering optical depth and consequently greater line width.

Two objects (IDs 58, 66) exhibit complex  $\text{H}\alpha$  profiles requiring multiple Gaussian components. In SRGe J175023.7+712857 (ID 58), the  $\text{H}\alpha$  profile resembles known double-peaked TDEs such as TDE 2018hyz (Hung et al. 2020; Short et al. 2020), TDE 2020zso (Wevers et al. 2022), and TDE 2020nov (Earl et al. 2025). The bluest and reddest peaks are  $\approx 4000$  km s $^{-1}$  shifted from rest-frame  $\text{H}\alpha$ , consistent with an accretion disk origin. In SRGe J213527.2-181635 (ID 66), both the +11 day and +33 day spectra show a blue component peaked  $\approx 4000$  km s $^{-1}$  blueward of rest-frame  $\text{H}\alpha$ , with no corresponding red component. Notably, both events show simple He II  $\lambda 4686$  profiles well-described by single Gaussians with FWHM  $\sim 2 \times 10^4$  km s $^{-1}$ , suggesting different dominant line production mechanisms for He II  $\lambda 4686$  and  $\text{H}\alpha$ .

In SRGe J131014.7+444319 (ID 26), the broad He II  $\lambda 4686$  and  $\text{H}\alpha$  have comparable widths. The +29 d spectrum shows a luminosity ratio  $L_{\text{He II}}/L_{\text{H}\alpha} \sim 2.9$ , which declined to  $\sim 1.1$  at +67 d. This evolution is consistent with the optically thick reprocessing picture of Roth et al. (2016), where  $\text{H}\alpha$  line strength is suppressed when the outer envelope radius is small, as expected in this X-ray-selected TDE.

In SRGe J011603.1+072258 (ID 5), the  $\text{H}\alpha$  component (FWHM  $\sim 4000$  km s $^{-1}$ ) is much narrower than the He II  $\lambda 4686$  line. We speculate that the  $\text{H}\alpha$  originates from a region farther from the black hole, similar to SRGe J153503.3+455054 discussed in §5.2.1.

## 5.3. Host properties

In this section, we discuss the host galaxy properties of our gold TDE sample. The silver sample is shown in figures for reference but is not the focus of our discussion.

<sup>6</sup> We cannot completely rule out line blending from Bowen fluorescence features, but since Bowen emission is more commonly observed in the TDE-H+He subtype rather than the TDE-He subtype (Gezari 2021), and given the deep  $\text{H}\alpha$  line luminosity upper limit, we consider this scenario less likely.

### 5.3.1. Host Colors versus Stellar Mass

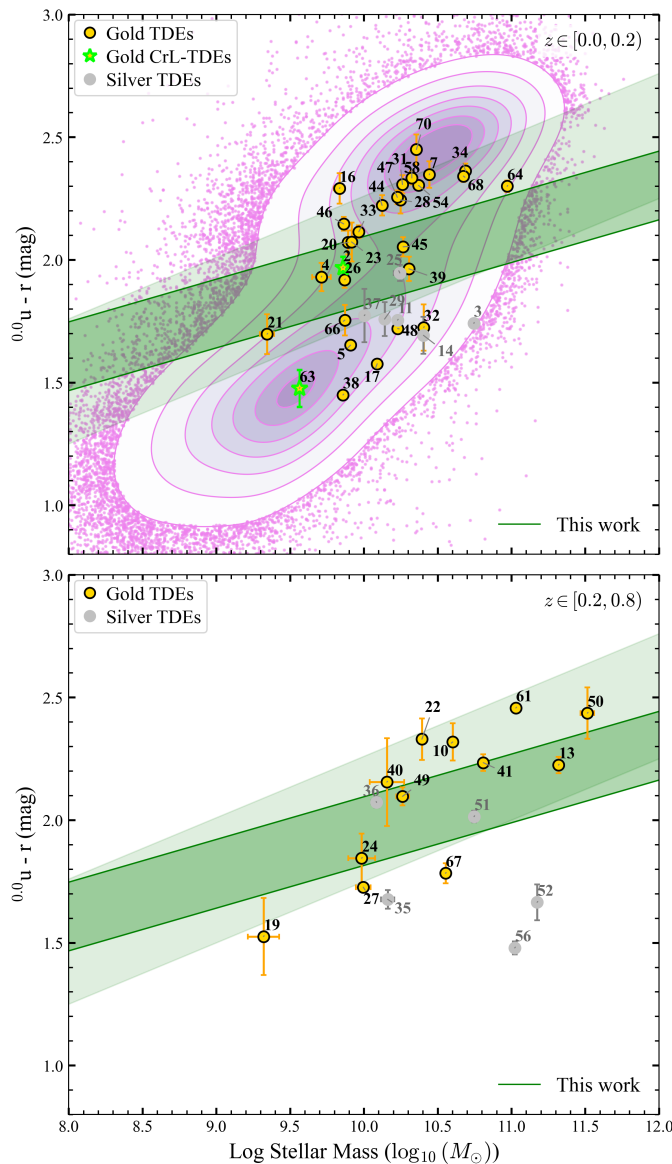


**Fig. 9:** Color–mass diagram for the final TDE host sample. The light-green band indicates the green-valley region defined by Schawinski et al. (2014). The darker-green band shows our empirically derived GV definition based on our SDSS comparison sample. Background contours are derived from our volume limited SDSS comparison galaxies (§4.4), shown at the 6.7–93.3% density levels.

Galaxy colors provide a simple diagnostic of star formation activity and quenching, allowing us to test whether TDE hosts preferentially reside in star-forming, quiescent, or transitional (green valley; GV) galaxies. Figure 9 presents the Galactic extinction corrected rest-frame  $u - r$  color as a function of stellar mass for our final TDE host sample. Both quantities are derived from the Prospector SED fits. Gold (yellow) and silver (grey) subsamples are distinguished, with CrL-TDEs (in the gold sample) highlighted separately in green. The background contours show the distribution of our volume limited SDSS comparison galaxies (see §4.4).

We define the GV empirically by identifying the density minimum in the color distribution between the “blue cloud” and “red sequence” galaxy populations in our comparison sample. A line

ear fit yields:

$$(u - r)_{\text{GV}} = 0.215 + 0.174 \times \log(M_*/M_\odot), \quad (2)$$

with a half-width  $\delta = 0.140$  mag estimated from the residual distribution. This approach directly traces the low-density transitional region.

To assess whether TDE hosts preferentially occupy the green valley, we perform a one-sided binomial test on our gold sample under the null hypothesis that TDE hosts are randomly drawn from the volume-limited SDSS comparison sample. The enrichment  $p$ -value is defined as

$$p_{\text{enrich}} = P(X \geq k \mid n, f_{\text{SDSS}}), \quad (3)$$

where  $k$  is the number of TDE hosts in the green valley,  $n$  is the total sample size, and  $f_{\text{SDSS}}$  is the green-valley fraction in the volume-limited SDSS comparison sample. We also report the fold enrichment  $\text{Fold} = f_{\text{TDE}}/f_{\text{SDSS}}$ . We adopt a stringent significance threshold of  $p_{\text{enrich}} < 0.001$  to claim genuine GV preference, given our modest sample size.

Quantitatively, 26.8% (11/41) of our gold sample fall within the tuned green valley (GV), with a 1.84-fold enrichment over our SDSS comparison sample. However, this enrichment does not meet the statistical significance for either the entire sample ( $p = 0.0295 > 0.001$ ) or the low redshift bin ( $p = 0.1191 > 0.001$ ), and we therefore do not find strong evidence for GV preference in X-ray-selected TDEs. The majority of the remaining TDEs are found in red sequence galaxies (46.3%, 19/41), with a smaller fraction in blue sequence galaxies (26.8%, 11/41). While the red sequence shows a modest 1.24-fold enhancement that is not statistically significant ( $p = 0.154$ ), we find no enrichment of TDEs in blue sequence galaxies relative to the SDSS comparison sample (0.56-fold). These results are consistent across both the full sample and the  $z = 0.0 - 0.2$  bin.

Our gold sample spans a broader  $u - r$  color and stellar mass range than previous studies (Sazonov et al. 2021; Grotova et al. 2025a), aligning more closely with the ZTF optical TDE sample (Yao et al. 2023), indicating a more diverse host population.

### 5.3.2. Lick indices: $H\delta_A$ versus $H\alpha$ EW

Previous work has shown that optically selected TDEs are frequently hosted by rare QBS or E+A galaxies with strong Balmer absorption and weak  $H\alpha$  emission. Specifically, using a sample of 8 optically-selected TDEs, French et al. (2016) found that quiescent galaxies with at least moderately strong Balmer absorption are over-represented among the TDE hosts by a factor of  $33^{+7}_{-11}$ . Graur et al. (2018) considered 35 TDE candidates selected by both X-ray and optical surveys, finding that the over-representation factor is  $18^{+8}_{-7}$ . More recently, using a sample of 19 ZTF TDEs, Hammerstein et al. (2021) found an over-representation factor of 16. The eROSITA selected sample (13 objects) presented by Sazonov et al. (2021) suggests a much weaker association with this class of hosts.

Figure 10 shows the Lick  $H\delta_A$  absorption index versus the  $H\alpha$  EW for our TDE host sample. Line indices and uncertainties are measured with pPXF (§4.2). Following French et al. (2016) and Hammerstein et al. (2021), we define the E+A region by  $H\delta_A - \sigma(H\delta_A) > 4.0$  and  $\text{EW}(H\alpha_{\text{em}}) < 3.0$  (solid box), and the QBS region by  $H\delta_A > 1.31$  and  $\text{EW}(H\alpha_{\text{em}}) < 3.0$  (dashed box).

First, we test the hypothesis that the distribution of our 40 gold TDE host galaxies in the Lick  $H\delta_A$  vs.  $\text{EW}(H\alpha)$  diagram is consistent with the comparison sample using a 2D Kolmogorov–Smirnov (KS) test (Fasano & Franceschini 1987). We do not include SRGe J163831.9+534018 (ID 50) in this analysis, as  $H\alpha$

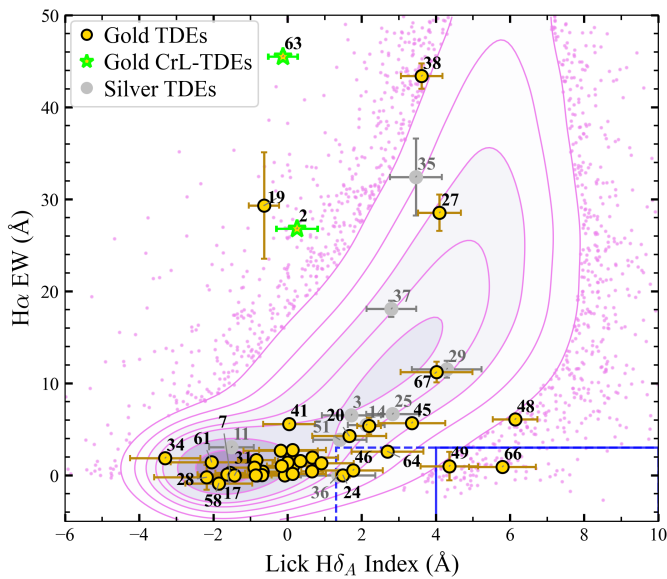


**Fig. 10:** Lick  $H\delta_A$  absorption index versus  $H\alpha$  emission equivalent width for our TDE host sample. The background shows the SDSS comparison sample with contours at  $\sigma$ -equivalent probability levels (6.7–93.3%). The solid and dashed boxes mark the E+A and QBS regions, respectively. To avoid label overlap, our gold and silver hosts near the origin are not individually labeled since many are clustered there.

is not available due to limited spectral coverage. The resulting  $p = 2.39 \times 10^{-9}$  strongly rejects the null hypothesis. This is not unexpected, as the  $EW(H\alpha)$  values of our gold TDE hosts are generally lower than the comparison sample, indicating suppressed star formation rates.

Next, we test whether our gold TDE hosts are overrepresented in the QBS and E+A regions using the binomial test described in §5.3.1. For the E+A region, 2 of 40 galaxies (5.0%) fall within the boundary, with  $F_{\text{old}} = 10.17$  and  $p_{\text{enrich}} = 1.66 \times 10^{-2}$ . This suggests enrichment but does not reach our statistical significance threshold. For the QBS region, 5 of 40 galaxies (12.5%) fall within the boundary, with  $F_{\text{old}} = 5.27$  and  $p_{\text{enrich}} = 2.48 \times 10^{-3}$ . This indicates QBS hosts enrichment but again does not reach our statistical significance threshold. Unlike the strong QBS preference seen previous works (French et al. 2016; Graur et al. 2018; Hammerstein et al. 2021), our X-ray-selected sample shows more modest enrichment.

### 5.3.3. Recent SFR versus Stellar Mass

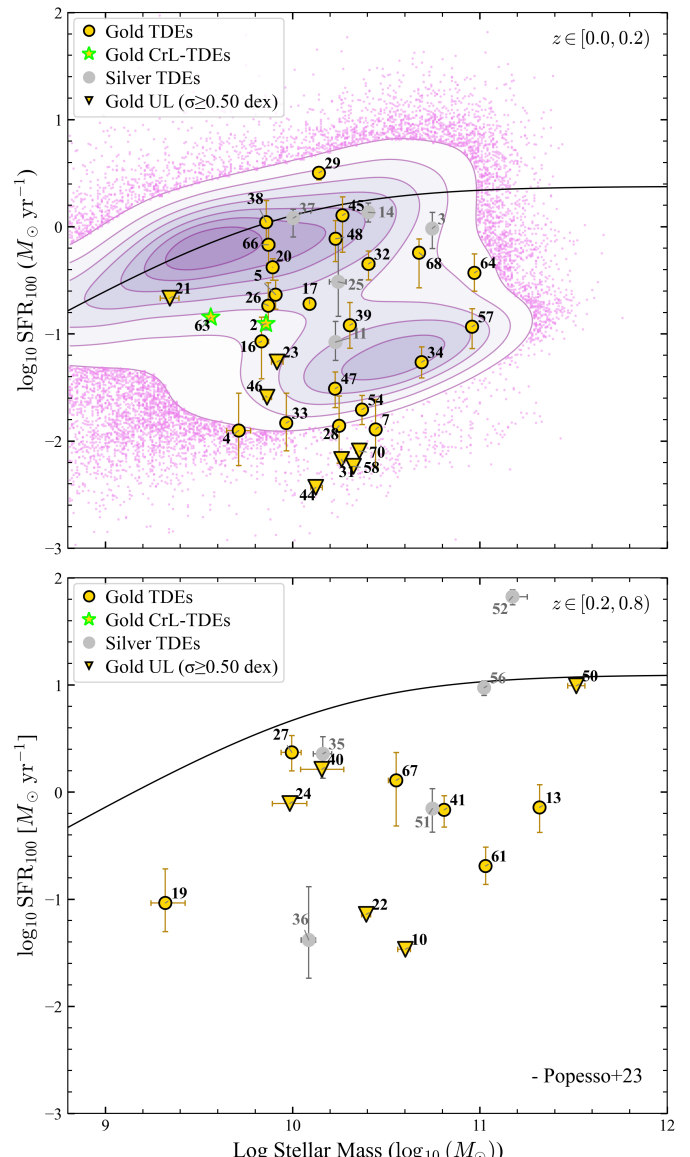
Unlike single-band tracers (e.g.,  $H\alpha$ , UV), our  $SFR_{100}$  are derived from Prospector’s nonparametric SFHs, providing a self-consistent 100 Myr average. Compared to the color-mass diagram (§5.3.1), the  $SFR_{100}$ – $M_*$  relation offers a complementary view of star formation in X-ray selected TDE hosts.

Figure 11 shows the SFR averaged over the past 100 Myr ( $SFR_{100}$ ) versus stellar mass from our Prospector fits. The background distribution shows the volume-limited SDSS comparison sample, and the solid black line indicates the star-forming main sequence from Popesso et al. (2023). Following Csizi et al. (2024), we split into two redshift bins ( $0.0 \leq z < 0.2$  and  $0.2 \leq z < 0.8$ ), which affects the main sequence.

Quantitatively, across both redshift bins, the vast majority of hosts fall below the star-forming main sequence (defined as lying below the main sequence of Popesso et al. 2023). In the low-

redshift bin ( $0.0 \leq z < 0.2$ ), 96.3% (26/27) of gold hosts are below the main sequence. In the high-redshift bin ( $0.2 \leq z < 0.8$ ), 100% (10/10) of gold hosts are below the main sequence. Most gold hosts have  $SFR_{100}$  values typically between  $10^{-3}$  and  $1 M_\odot \text{ yr}^{-1}$ , consistent with suppressed or quenching star formation. SRGe J170139.0-085911 (ID 52) appears as an outlier above the sequence, though its Prospector fit may likely overestimate the SFR.

X-ray-selected TDE hosts predominantly avoid the star-forming main sequence. This result is consistent with the color–mass and line-index diagnostics, which also place most hosts in transitional or weakly star-forming regimes rather than strongly star-forming disks. The preference for hosts below the main sequence is expected, as dustier star-forming galaxies can strongly absorb soft X-ray emission, making TDEs harder to detect (Panagiotou et al. 2023).



**Fig. 11:** Star formation rate averaged over the past 100 Myr ( $SFR_{100}$ ) versus stellar mass for our TDE hosts, split into two redshift bins ( $0.0 \leq z < 0.2$  and  $0.2 \leq z < 0.8$ ). The pink background shows the volume-limited SDSS comparison sample described with SFR measurement. The solid black line marks the redshift-dependent star-forming main sequence from Popesso et al. (2023).

## 6. Conclusion

We present uniform Keck-I/LRIS observations, host galaxy modeling, as well as light curve and spectroscopic analysis for 70 TDE candidates selected from eROSITA all-sky surveys in the Eastern Galactic hemisphere. We develop a robust method for removing AGN interlopers, yielding a final sample of 52 TDEs with redshifts of  $0.018 \leq z \leq 0.714$ . The final TDE sample includes 41 high-confidence (gold) events and 11 lower-confidence (silver) events, representing the largest systematically selected X-ray TDE sample to date. The main results for our gold sample are:

- The vast majority of X-ray-selected TDEs are intrinsically X-ray-bright, with 38/41 (93%) exhibiting  $L_{X,peak} > L_{opt,peak}$  (see Figure 6).
- X-ray emission typically peaks 3–276 days (68% range) after optical peak in events with detected optical flares (Figure 7), confirming that delayed X-ray brightening is common to the TDE population.
- We identify TDE-associated spectral features in eight events: two coronal-line TDEs (§4.3.2) and six with prominent broad emission lines (§4.3.4). The uniformly broad He II  $\lambda 4686$  emission (FWHM  $\sim 2 \times 10^4 \text{ km s}^{-1}$ ) indicates high electron scattering optical depth, while the diverse H $\alpha$  line profiles suggest multiple emission mechanisms (§5.2).
- X-ray-selected TDE hosts show modest overrepresentation in green valley (1.8 $\times$ ; §5.3.1) and quiescent Balmer-strong (5.3 $\times$ ; §5.3.2) galaxies, which are significantly weaker than optical and pre-eROSITA X-ray samples. This demonstrates that eROSITA TDE hosts span a broader range of star formation histories than previous samples of TDE hosts.
- Our TDE hosts generally exhibit lower star formation rates relative to the star-forming main sequence (§5.3.3). This might be explained by the fact that star-forming galaxies contain more dust that strongly absorb soft X-rays, making TDE selection in the soft X-ray band challenging.

This work represents a substantial and well-characterized subsample of eROSITA-RU-selected TDEs. A forthcoming study will present the complete eROSITA-RU TDE sample with uniform analysis. The observed diversity in both TDE properties and host galaxy characteristics presented here should guide future theoretical models of TDE emission mechanisms and their dependence on environment.

**Acknowledgements.** This work uses data obtained with eROSITA telescope on-board SRG observatory. The SRG observatory was built by Roskosmos with the participation of the Deutsches Zentrum für Luft- und Raumfahrt (DLR). The SRG/eROSITA X-ray telescope was built by a consortium of German Institutes led by MPE, and supported by DLR. The SRG spacecraft was designed, built, launched and is operated by the Lavochkin Association and its subcontractors. The science data were downlinked via the Deep Space Network Antennae in Bear Lakes, Ussurijsk, and Baykonur, funded by Roskosmos. The eROSITA data used in this work were processed using the eSASS software system developed by the German eROSITA consortium and proprietary data reduction and analysis software developed by the Russian eROSITA Consortium. MG and SS acknowledge support by the Ministry of Science and Higher Education grant 075-15-2024-647. Some of the data presented herein were obtained at Keck Observatory, which is a private 501(c)3 non-profit organization operated as a scientific partnership among the California Institute of Technology, the University of California, and the National Aeronautics and Space Administration. The Observatory was made possible by the generous financial support of the W. M. Keck Foundation. The authors wish to recognize and acknowledge the very significant cultural role and reverence that the summit of Maunakea has always had within the Native Hawaiian community. We are most fortunate to have the opportunity to conduct observations from this mountain.

## References

Alexander, K. D., van Velzen, S., Horesh, A., & Zauderer, B. A. 2020, *Space Sci. Rev.*, 216, 81

Andalman, Z. L., Liska, M. T. P., Tchekhovskoy, A., Coughlin, E. R., & Stone, N. 2022, *MNRAS*, 510, 1627

Antonucci, R. 1993, *ARA&A*, 31, 473

Arcavi, I., Gal-Yam, A., Sullivan, M., et al. 2014, *ApJ*, 793, 38

Bade, N., Komossa, S., & Dahlem, M. 1996, *A&A*, 309, L35

Baldwin, J. A., Phillips, M. M., & Terlevich, R. 1981, *PASP*, 93, 5

Beck, R., Szapudi, I., Flewelling, H., et al. 2021, *MNRAS*, 500, 1633

Bellm, E. C., Kulkarni, S. R., Graham, M. J., et al. 2019, *PASP*, 131, 018002

Blanton, M. R., Schlegel, D. J., Strauss, M. A., et al. 2005, *AJ*, 129, 2562

Brandt, W. N., Pounds, K. A., & Fink, H. 1995, *MNRAS*, 273, L47

Brinchmann, J., Charlot, S., White, S. D. M., et al. 2004, *MNRAS*, 351, 1151

Callow, J., Graur, O., Clark, P., et al. 2024, *MNRAS*, 535, 1095

Cao, Z., Jonker, P. G., Pasham, D. R., et al. 2024, *ApJ*, 970, 89

Cappellari, M. 2023, *MNRAS*, 526, 3273

Cardelli, J. A., Clayton, G. C., & Mathis, J. S. 1989, *ApJ*, 345, 245

Chambers, K. C., Magnier, E. A., Metcalfe, N., et al. 2016, *arXiv e-prints*, arXiv:1612.05560

Charalampopoulos, P., Leloudas, G., Malesani, D. B., et al. 2022, *Astronomy & Astrophysics*, 659, A34

Charlot, S. & Fall, S. M. 2000, *ApJ*, 539, 718

Cid Fernandes, R., Stasińska, G., Mateus, A., & Vale Asari, N. 2011, *MNRAS*, 413, 1687

Clark, P., Callow, J., Graur, O., et al. 2025, *MNRAS*, 540, 871

Conroy, C. & Gunn, J. E. 2010, *FSPS: Flexible Stellar Population Synthesis, Astrophysics Source Code Library*, record ascl:1010.043

Csizér, B., Tortorelli, L., Siudek, M., et al. 2024, *Astronomy & Astrophysics*, 689, A37

Cutri, R. M., Wright, E. L., Conrow, T., et al. 2013, *Explanatory Supplement to the AllWISE Data Release Products, Explanatory Supplement to the AllWISE Data Release Products*, by R. M. Cutri et al.

Cutri, R. M., Wright, E. L., Conrow, T., et al. 2021, *VizieR Online Data Catalog: AllWISE Data Release (Cutri+ 2013)*, *VizieR On-line Data Catalog: II/328*. Originally published in: IPAC/Caltech (2013)

De Colle, F. & Lu, W. 2020, *New A Rev.*, 89, 101538

DESI Collaboration, Abdul-Karim, M., Adame, A. G., et al. 2025, *arXiv e-prints*, arXiv:2503.14745

Dey, A., Schlegel, D. J., Lang, D., et al. 2019, *AJ*, 157, 168

Draine, B. T. & Li, A. 2007, *ApJ*, 657, 810

Earl, N., French, K. D., Ramirez-Ruiz, E., et al. 2025, *ApJ*, 983, 28

Eisenhardt, P. R. M., Marocco, F., Fowler, J. W., et al. 2020, *ApJS*, 247, 69

Evans, P. A., Nixon, C. J., Campana, S., et al. 2023, *Nature Astronomy*, 7, 1368

Fasano, G. & Franceschini, A. 1987, *Monthly Notices of the Royal Astronomical Society*, 225, 155

Filippenko, A. V. 1996, in *Astronomical Society of the Pacific Conference Series*, Vol. 103, *The Physics of Liners in View of Recent Observations*, ed. M. Eracleous, A. Koratkar, C. Leitherer, & L. Ho, 17

Flewelling, H. A., Magnier, E. A., Chambers, K. C., et al. 2020, *ApJS*, 251, 7

French, K. D., Arcavi, I., & Zabludoff, A. 2016, *ApJ*, 818, L21

Gaia Collaboration, Vallenari, A., Brown, A. G. A., et al. 2023, *A&A*, 674, A1

Gallazzi, A., Charlot, S., Brinchmann, J., White, S. D. M., & Tremonti, C. A. 2005, *MNRAS*, 362, 41

Gezari, S. 2021, *ARA&A*, 59, 21

Graham, M. J., Kulkarni, S. R., Bellm, E. C., et al. 2019, *PASP*, 131, 078001

Graur, O., French, K. D., Zahid, H. J., et al. 2018, *ApJ*, 853, 39

Grotova, I., Rau, A., Baldini, P., et al. 2025a, *A&A*, 697, A159

Grotova, I., Rau, A., Salvato, M., et al. 2025b, *A&A*, 693, A62

Grupe, D., Beuerman, K., Mannheim, K., et al. 1995, *A&A*, 300, L21

Guolo, M., Gezari, S., Yao, Y., et al. 2024a, *ApJ*, 966, 160

Guolo, M., Pasham, D. R., Zajáček, M., et al. 2024b, *Nature Astronomy*, 8, 347

Hammerstein, E., Gezari, S., van Velzen, S., et al. 2021, *The Astrophysical Journal Letters*, 908, L20

Hammerstein, E., van Velzen, S., Gezari, S., et al. 2023, *ApJ*, 942, 9

Hannah, C. H., Stone, N. C., Seth, A. C., & van Velzen, S. 2025, *ApJ*, 988, 29

Heckman, T. M. 1980, *A&A*, 87, 152

Hinkle, J. T., Shappee, B. J., & Holoiien, T. W.-S. 2024, *MNRAS*, 528, 4775

Ho, A. Y. Q., Yao, Y., Matsumoto, T., et al. 2025, *ApJ*, 989, 54

Ho, L. C., Filippenko, A. V., & Sargent, W. L. W. 1993, *ApJ*, 417, 63

Hung, T., Cenko, S. B., Roth, N., et al. 2019, *The Astrophysical Journal*, 879, 119

Hung, T., Foley, R. J., Ramirez-Ruiz, E., et al. 2020, *ApJ*, 903, 31

Jiang, N., Wang, T., Hu, X., et al. 2021, *ApJ*, 911, 31

Johnson, B. D., Leja, J., Conroy, C., & Speagle, J. S. 2021a, *ApJS*, 254, 22

Johnson, B. D., Leja, J., Conroy, C., & Speagle, J. S. 2021b, *ApJS*, 254, 22

Kass, R. E. & Raftery, A. E. 1995, *J. Am. Statist. Assoc.*, 90, 773

Kauffmann, G., Heckman, T. M., Tremonti, C., et al. 2003a, *MNRAS*, 346, 1055

Kauffmann, G., Heckman, T. M., White, S. D. M., et al. 2003b, MNRAS, 341, 33

Kewley, L. J., Groves, B., Kauffmann, G., & Heckman, T. 2006, MNRAS, 372, 961

Khabibullin, I., Medvedev, P., Churazov, E., et al. 2020a, The Astronomer's Telegram, 13499, 1

Khabibullin, I., Sazonov, S., & Sunyaev, R. 2014, MNRAS, 437, 327

Khabibullin, I., Sunyaev, R., Churazov, E., et al. 2020b, The Astronomer's Telegram, 13494, 1

Khorunzhev, G. A., Sazonov, S. Y., Medvedev, P. S., et al. 2022, Astronomy Letters, 48, 767

Khorunzhev, G. A., Sazonov, S. Y., Medvedev, P. S., et al. 2024, Astronomy Letters, 50, 744

Komossa, S. 2015, Journal of High Energy Astrophysics, 7, 148

Komossa, S. & Greiner, J. 1999, A&A, 349, L45

Komossa, S., Zhou, H., Wang, T., et al. 2008, ApJ, 678, L13

Kriek, M. & Conroy, C. 2013, ApJ, 775, L16

Kumar, H., Berger, E., Hiramatsu, D., et al. 2024, AT2023vto: An Exceptionally Luminous Helium Tidal Disruption Event from a Massive Star

Liu, Z., Malyali, A., Krumpe, M., et al. 2023, A&A, 669, A75

Lorah, J. & Womack, A. 2019, Behavior Research Methods, 51, 440

Malyali, A., Liu, Z., Merloni, A., et al. 2023, MNRAS, 520, 4209

Malyali, A., Rau, A., Bonnerot, C., et al. 2024, MNRAS, 531, 1256

Martin, D. C., Fanson, J., Schiminovich, D., et al. 2005, ApJ, 619, L1

Masci, F. J., Laher, R. R., Rusholme, B., et al. 2023, arXiv e-prints, arXiv:2305.16279

Masci, F. J., Laher, R. R., Rusholme, B., et al. 2019, PASP, 131, 018003

Medvedev, P. S., Gilfanov, M. R., Sazonov, S. Y., Sunyaev, R. A., & Khorunzhev, G. A. 2022, Astronomy Letters, 48, 735

Mendel, J. T., Simard, L., Palmer, M., Ellison, S. L., & Patton, D. R. 2014, ApJS, 210, 3

Million, C., Fleming, S. W., Shiao, B., et al. 2016, ApJ, 833, 292

Mondal, S. & French, K. D. 2025, arXiv e-prints, arXiv:2508.03889

Nenkova, M., Sirocky, M. M., Nikutta, R., Ivezić, Ž., & Elitzur, M. 2008, ApJ, 685, 160

Newsome, M., Arcavi, I., Howell, D. A., et al. 2024, ApJ, 977, 258

Nicholl, M., Blanchard, P. K., Berger, E., et al. 2019, Monthly Notices of the Royal Astronomical Society, 488, 1878

Nicholl, M., Wevers, T., Oates, S. R., et al. 2020, MNRAS, 499, 482

Nikutta, R., Fitzpatrick, M., Scott, A., & Weaver, B. A. 2020, Astronomy and Computing, 33, 100411

Oke, J. B., Cohen, J. G., Carr, M., et al. 1995, PASP, 107, 375

Onori, F., Cannizzaro, G., Jonker, P. G., et al. 2022, MNRAS, 517, 76

Panagiotou, C., De, K., Masterson, M., et al. 2023, The Astrophysical Journal Letters, 948, L5

Phinney, E. S. 1989, in IAU Symposium, Vol. 136, The Center of the Galaxy, ed. M. Morris, 543

Popesso, P., Concas, A., Cresci, G., et al. 2023, MNRAS, 519, 1526

Predehl, P., Andritschke, R., Arefiev, V., et al. 2021, A&A, 647, A1

Price, D. J., Liptai, D., Mandel, I., et al. 2024, ApJ, 971, L46

Pulatova, N. G., Rubtsov, E., Chilingarian, I. V., et al. 2025, Optical Emission-Line Properties of eROSITA-selected SDSS-V Galaxies

Rees, M. J. 1988, Nature, 333, 523

Roth, N. & Kasen, D. 2018, ApJ, 855, 54

Roth, N., Kasen, D., Guillotin-Ruiz, E. 2016, The Astrophysical Journal, 827, 3

Roth, N., Rossi, E. M., Krolik, J., et al. 2020, Space Sci. Rev., 216, 114

Ryu, T., Krolik, J., Piran, T., Noble, S. C., & Avara, M. 2023, ApJ, 957, 12

Saxton, R., Komossa, S., Auchettl, K., & Jonker, P. G. 2020, Space Sci. Rev., 216, 85

Sazonov, S., Gilfanov, M., Medvedev, P., et al. 2021, MNRAS, 508, 3820

Schawinski, K., Urry, C. M., Simmons, B. D., et al. 2014, Monthly Notices of the Royal Astronomical Society, 440, 889–907

Schlegel, D. J., Finkbeiner, D. P., & Davis, M. 1998, ApJ, 500, 525

Shingles, L., Smith, K. W., Young, D. R., et al. 2021, Transient Name Server AstroNote, 7, 1

Short, P., Lawrence, A., Nicholl, M., et al. 2023, MNRAS, 525, 1568

Short, P., Nicholl, M., Lawrence, A., et al. 2020, MNRAS, 498, 4119

Singh, R., van de Ven, G., Jahnke, K., et al. 2013, A&A, 558, A43

Skrutskie, M. F., Cutri, R. M., Stiening, R., et al. 2006, AJ, 131, 1163

Smith, K. W., Smartt, S. J., Young, D. R., et al. 2020, PASP, 132, 085002

Somalwar, J. J., Ravi, V., & Lu, W. 2025, ApJ, 983, 159

Speagle, J. S. 2020, MNRAS, 493, 3132

Steinberg, E. & Stone, N. C. 2024, Nature, 625, 463

Stern, D., Assef, R. J., Benford, D. J., et al. 2012, ApJ, 753, 30

Stern, J. & Laor, A. 2012, Monthly Notices of the Royal Astronomical Society, 426, 2703–2718

Stone, N. C., Vasiliev, E., Kesden, M., et al. 2020, Space Sci. Rev., 216, 35

Stoughton, C., Lupton, R. H., Bernardi, M., et al. 2002, AJ, 123, 485

Sunyaev, R., Arefiev, V., Babushkin, V., et al. 2021, A&A, 656, A132

Sutherland, W. & Saunders, W. 1992, MNRAS, 259, 413

Tonry, J. L., Denneau, L., Heinze, A. N., et al. 2018, PASP, 130, 064505

Tremonti, C. A., Heckman, T. M., Kauffmann, G., et al. 2004, ApJ, 613, 898

Ueda, Y., Hashimoto, Y., Ichikawa, K., et al. 2015, ApJ, 815, 1

van Velzen, S., Gezari, S., Hammerstein, E., et al. 2021, ApJ, 908, 4

Vazdekis, A., Koleva, M., Ricciardelli, E., Röck, B., & Falcón-Barroso, J. 2016, MNRAS, 463, 3409

Wang, T.-G., Zhou, H.-Y., Komossa, S., et al. 2012, ApJ, 749, 115

Wang, T.-G., Zhou, H.-Y., Wang, L.-F., Lu, H.-L., & Xu, D. 2011, ApJ, 740, 85

Wevers, T. 2020, MNRAS, 497, L1

Wevers, T., Guolo, M., Pasham, D. R., et al. 2024, ApJ, 963, 75

Wevers, T., Nicholl, M., Guolo, M., et al. 2022, A&A, 666, A6

Wright, E. L., Eisenhardt, P. R. M., Mainzer, A. K., et al. 2010, AJ, 140, 1868

Yao, Y. 2023, PhD thesis, California Institute of Technology, Division of Physics, Mathematics and Astronomy

Yao, Y., De, K., Kasliwal, M. M., et al. 2020, ApJ, 900, 46

Yao, Y., Lu, W., Guolo, M., et al. 2022, The Astrophysical Journal, 937, 8

Yao, Y., Lu, W., Harrison, F., et al. 2024, ApJ, 965, 39

Yao, Y., Miller, A. A., Kulkarni, S. R., et al. 2019, ApJ, 886, 152

Yao, Y., Ravi, V., Gezari, S., et al. 2023, ApJ, 955, L6

## Appendix A: Supplementary Figures

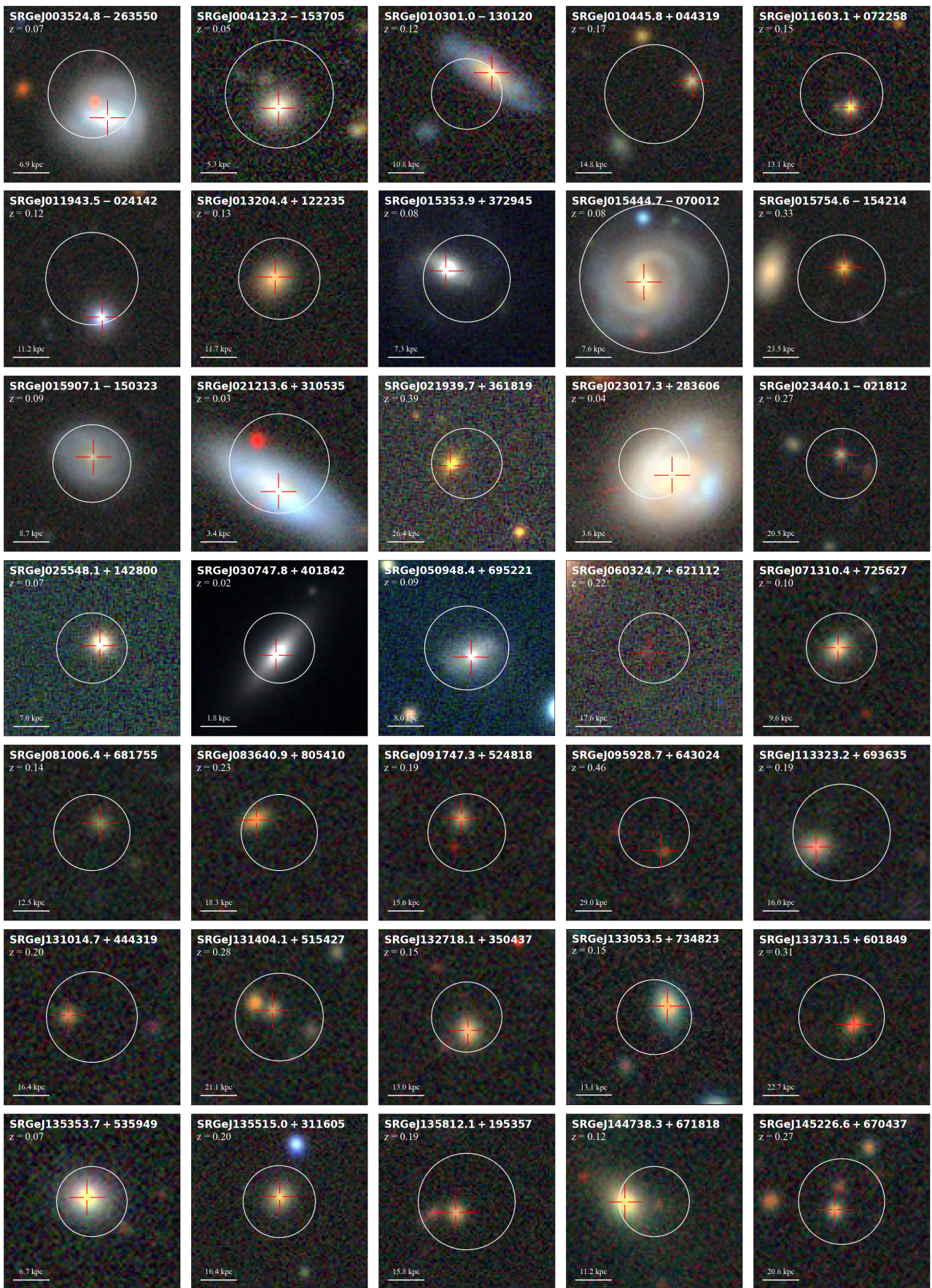
Figures A.1 and A.2 show the LS color images of the host galaxies of the 70 TDE candidates.

Figures A.3, A.4, A.5, and A.6 show the forced photometry light curves of the host galaxy nuclei of the 70 TDE candidates. Note that two optical spectra obtained in June 2025 (IDs 55, 58) are beyond the time range of the x-axis. For ID 47, since the optical flare was detected during ZTF reference image building, we perform baseline correction following [Yao et al. \(2019\)](#).

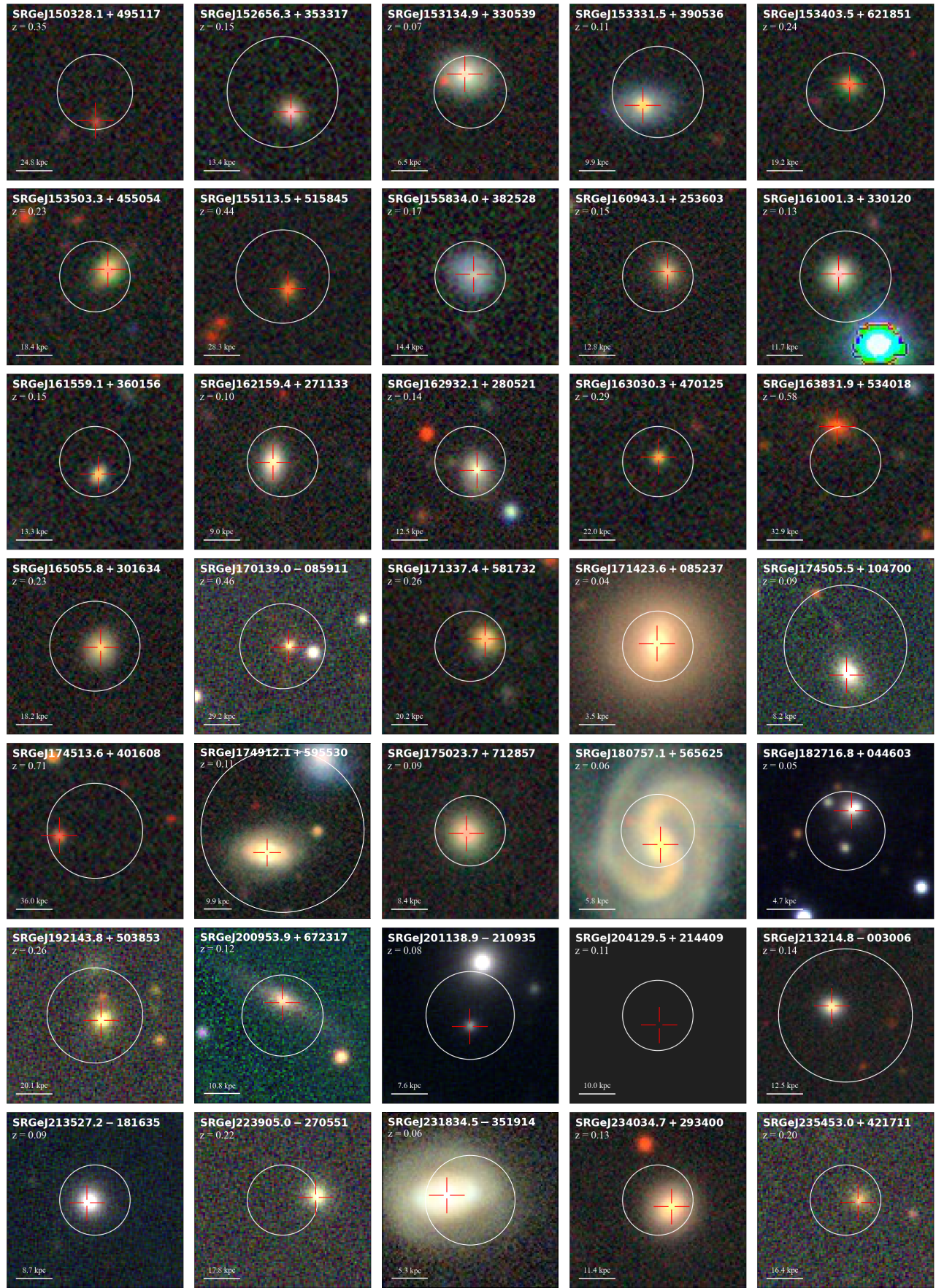
Figures A.7 and A.8 show the Prospector SED fitting results of the host galaxies of our gold and silver samples.

## Appendix B: Supplementary Tables

Table B.1 shows the properties of broad TDE emission lines detected in our Keck-I/LRIS spectra.



**Fig. A.1:** Legacy Survey DR9 co-added and PS1 color cutouts (100 × 100 pixels) of the eROSITA TDE host-galaxy associations. The eROSITA 98% confidence position is shown as a white circle, and the optical counterpart is marked with an open red cross.

**Fig. A.2:** Continued figure of Fig. A.1.

**Table B.1:** Properties of emission lines in TDE spectra modeled with Gaussian profiles.

| TDE class                            | Phase (days) | Line                        | $\lambda_0$ (Å)     | EW (Å)            | FWHM (km s <sup>-1</sup> ) | Luminosity (10 <sup>38</sup> erg s <sup>-1</sup> ) |
|--------------------------------------|--------------|-----------------------------|---------------------|-------------------|----------------------------|--|
| <b>SRGe J011603.1+072258 (ID 5)</b>  |              |                             |                     |                   |                            |  |
| TDE-H+He                             | 40           | He II $\lambda 4686$        | 4685.7              | 72.68 $\pm$ 13.24 | 19381 $\pm$ 969            | 1344 $\pm$ 44.39                                   |
|                                      |              | H $\beta$ broad             | 4861.3              | 6.33 $\pm$ 1.19   | 2435 $\pm$ 122             | 72.60 $\pm$ 18.42                                  |
|                                      |              | H $\alpha$ broad            | 6562.8              | 11.95 $\pm$ 2.45  | 3758 $\pm$ 188             | 96.16 $\pm$ 17.11                                  |
|                                      | 65           | He II $\lambda 4686$        | —                   | —                 | —                          | < 24.89  |
|                                      |              | H $\alpha$ broad            | —                   | —                 | —                          | < 25.32  |
|                                      |              | H $\beta$ broad             | —                   | —                 | —                          | < 19.51  |
| <b>SRGe J131014.7+444319 (ID 26)</b> |              |                             |                     |                   |                            |  |
| TDE-H+He                             | 29           | He II $\lambda 4686$        | 4685.7              | 40.69 $\pm$ 6.43  | 17263 $\pm$ 1726           | 1353 $\pm$ 203                                     |
|                                      |              | H $\beta$ broad             | 4861.3              | 12.44 $\pm$ 1.92  | 11616 $\pm$ 1162           | 367.3 $\pm$ 55.1                                   |
|                                      |              | H $\alpha$ broad            | 6562.8              | 25.13 $\pm$ 3.90  | 11235 $\pm$ 1124           | 473.7 $\pm$ 51.72                                  |
|                                      | 67           | Bowen blend                 | 4566.1 $\pm$ 36.5   | 9.12 $\pm$ 1.33   | 5639 $\pm$ 564             | 299.1 $\pm$ 44.87                                  |
|                                      |              | He II $\lambda 4686$        | 4685.7              | 33.91 $\pm$ 5.14  | 12779 $\pm$ 1278           | 690.7 $\pm$ 103.6                                  |
|                                      |              | H $\beta$ broad             | 4861.3              | 22.44 $\pm$ 3.46  | 11616 $\pm$ 1026           | 408.3 $\pm$ 61.25                                  |
|                                      | 244          | H $\alpha$ broad            | 6562.8              | 48.07 $\pm$ 7.61  | 11103 $\pm$ 1110           | 606.7 $\pm$ 51.43                                  |
|                                      |              | Bowen blend                 | 4600.3 $\pm$ 27.5   | 9.27 $\pm$ 1.50   | 4220 $\pm$ 422             | 184.5 $\pm$ 27.67                                  |
|                                      |              | He II $\lambda 4686$        | —                   | —                 | —                          | < 31.30  |
| <b>SRGe J153331.5+390536 (ID 39)</b> |              |                             |                     |                   |                            |  |
| —                                    | 142          | He II $\lambda 4686$        | 4685.7              | 25.76 $\pm$ 4.99  | 28474 $\pm$ 1424           | 188.7 $\pm$ 150.5                                  |
|                                      |              | H $\alpha$ broad            | 6541.13 $\pm$ 22.36 | 3.83 $\pm$ 1.95   | 3758 $\pm$ 189             | 42.30 $\pm$ 21.15                                  |
| <b>SRGe J153503.3+455054 (ID 41)</b> |              |                             |                     |                   |                            |  |
| TDE-H?                               | 303          | H $\alpha$ broad            | 6562.8              | 9.95 $\pm$ 1.52   | 2679 $\pm$ 134             | 912.5 $\pm$ 136.2                                  |
|                                      |              | He II $\lambda 4686$        | —                   | —                 | —                          | < 165.0  |
| <b>SRGe J175023.7+712857 (ID 58)</b> |              |                             |                     |                   |                            |  |
| TDE-H+He                             | 182          | He II $\lambda 4686$        | 4685.7              | 25.77 $\pm$ 4.86  | 22597 $\pm$ 1130           | 692.6 $\pm$ 142.9                                  |
|                                      |              | H $\alpha$ blue             | 6477.2 $\pm$ 5.7    | 3.08 $\pm$ 2.34   | 1255 $\pm$ 815             | 85.28 $\pm$ 64.21                                  |
|                                      |              | H $\alpha$ broad            | 6525.0 $\pm$ 10.8   | 8.76 $\pm$ 7.91   | 5365 $\pm$ 3752            | 241.2 $\pm$ 216.5                                  |
|                                      |              | H $\alpha$ red <sub>1</sub> | 6594.4 $\pm$ 7.2    | 3.48 $\pm$ 2.36   | 1326 $\pm$ 742             | 94.91 $\pm$ 63.54                                  |
|                                      |              | H $\alpha$ red <sub>2</sub> | 6651.6 $\pm$ 8.2    | 6.85 $\pm$ 3.22   | 2278 $\pm$ 783             | 184.9 $\pm$ 85.09                                  |
|                                      | 1333         | He II $\lambda 4686$        | —                   | —                 | —                          | < 26.57  |
|                                      |              | H $\alpha$                  | —                   | —                 | —                          | < 31.56  |
| <b>SRGe J213527.2-181635 (ID 66)</b> |              |                             |                     |                   |                            |  |
| TDE-H+He                             | 11           | He II $\lambda 4686$        | 4690.0 $\pm$ 2.67   | 39.45 $\pm$ 7.52  | 30132 $\pm$ 3366           | 2420 $\pm$ 674                                     |
|                                      |              | H $\alpha$ broad            | 6588.2 $\pm$ 110.4  | 20.20 $\pm$ 4.29  | 12029 $\pm$ 4033           | 1018 $\pm$ 209                                     |
|                                      |              | H $\alpha$ rest             | 6567.1 $\pm$ 17.2   | 3.82 $\pm$ 2.35   | 1909 $\pm$ 1380            | 193 $\pm$ 119                                      |
|                                      |              | H $\alpha$ blue             | 6472.6 $\pm$ 20.8   | 2.69 $\pm$ 2.02   | 2238 $\pm$ 1289            | 127 $\pm$ 105                                      |
|                                      |              | He II $\lambda 4686$        | 4690.00 $\pm$ 0.85  | 15.18 $\pm$ 6.32  | 22598 $\pm$ 4185           | 604.2 $\pm$ 251.5                                  |
|                                      | 33           | H $\alpha$ broad            | 6562.8 $\pm$ 126.5  | 14.90 $\pm$ 4.98  | 9265 $\pm$ 3765            | 450 $\pm$ 151                                      |
|                                      |              | H $\alpha$ rest             | 6567.1 $\pm$ 19.7   | 3.67 $\pm$ 1.89   | 1855 $\pm$ 209             | 111 $\pm$ 57                                       |
|                                      |              | H $\alpha$ blue             | 6472.6 $\pm$ 18.9   | 2.84 $\pm$ 1.45   | 2047 $\pm$ 417             | 83.3 $\pm$ 53.9                                    |
|                                      |              | He II $\lambda 4686$        | —                   | —                 | —                          | < 43.57  |
|                                      |              | H $\alpha$ broad            | —                   | —                 | —                          | < 52.19  |
| <b>SRGe J235453.0+421711 (ID 70)</b> |              |                             |                     |                   |                            |  |
| TDE-He                               | 197          | He II $\lambda 4686$        | 4515.7 $\pm$ 12.5   | 69.97 $\pm$ 13.48 | 24262 $\pm$ 7809           | 966.9 $\pm$ 179.2                                  |
|                                      |              | H $\beta$ broad             | 4861.3              | 5.73 $\pm$ 2.22   | 1595 $\pm$ 607             | 79.88 $\pm$ 32.15                                  |
|                                      |              | H $\alpha$ broad            | —                   | —                 | —                          | < 48.81  |

**Notes.** For SRGe J235453.0+421711 (ID 70), the skewness of He II  $\lambda 4686$  line is  $-0.36 \pm 0.29$ . Given the non-detection of H $\alpha$ , we classify this object as TDE-He. While a Gaussian centered on H $\beta$  is favored by BIC ( $\Delta\text{BIC} = 11.42 > 10$ ), we note that this line detection is of very low significance ( $2.6\sigma$ ). Similarly, given the low significance of line EWs of SRGe J153331.5+390536 (ID 39), we do not assign a spectroscopic subtype for this event.

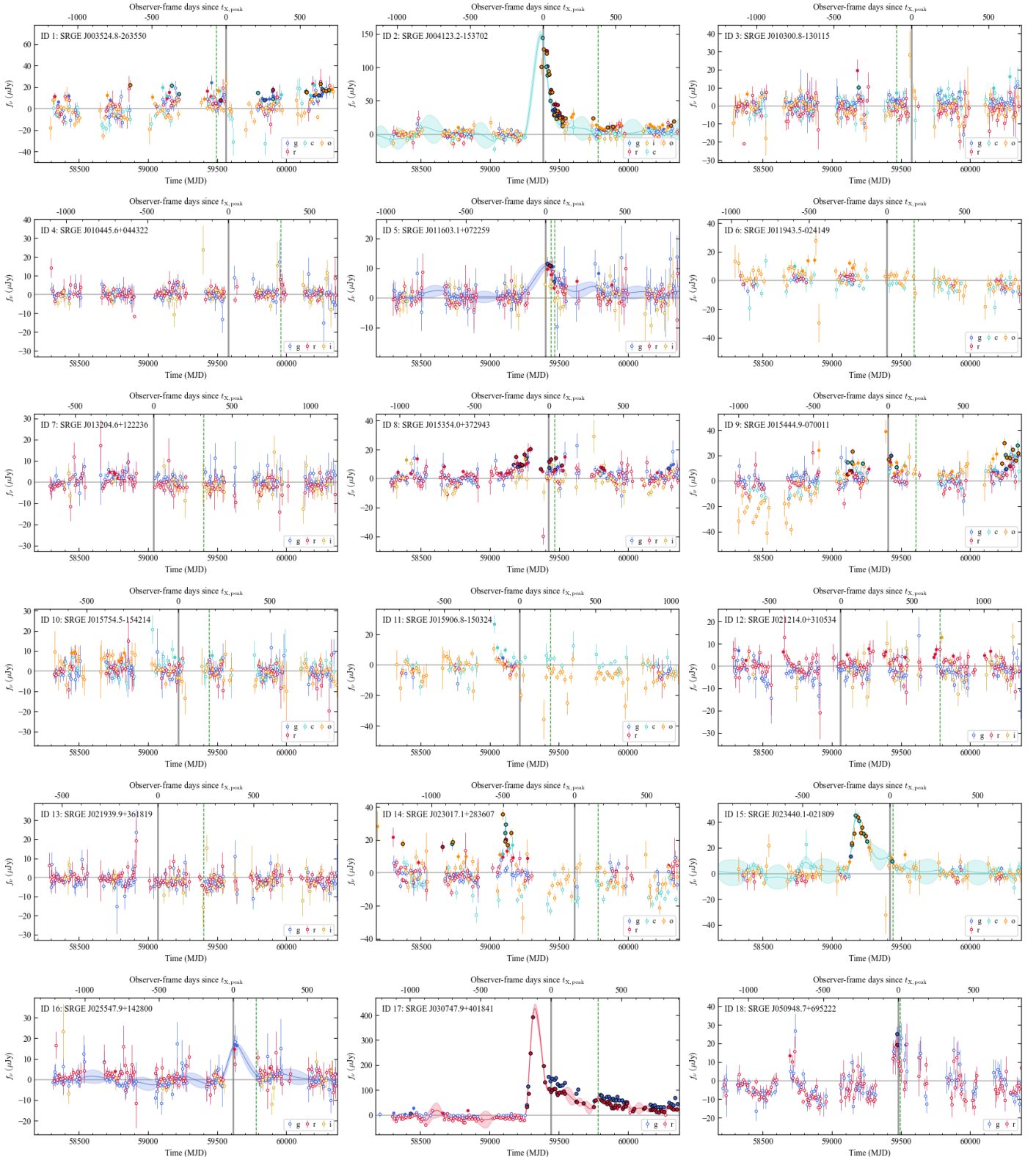


**Fig. A.3:** ZTF and ATLAS differential photometry performed at the centroids of the host galaxies. Data points with  $< 3\sigma$  significance are shown as hollow circles,  $> 3\sigma$  as solid circles, and  $> 5\sigma$  are further highlighted with black edges. Spectroscopic observation epochs are marked with vertical dashed green lines. Epochs of X-ray peak are marked with vertical solid gray lines. Data are binned in 10-day intervals for clarity. For TDEs with detected optical flares, we show Gaussian process model fits following the procedures described in Appendix B.4 of Yao et al. (2020). Models are fitted to the band with either the smallest photometric uncertainties or the best temporal coverage. The x-axis spans from 2018 March 1 to 2024 March 1 for all sources.

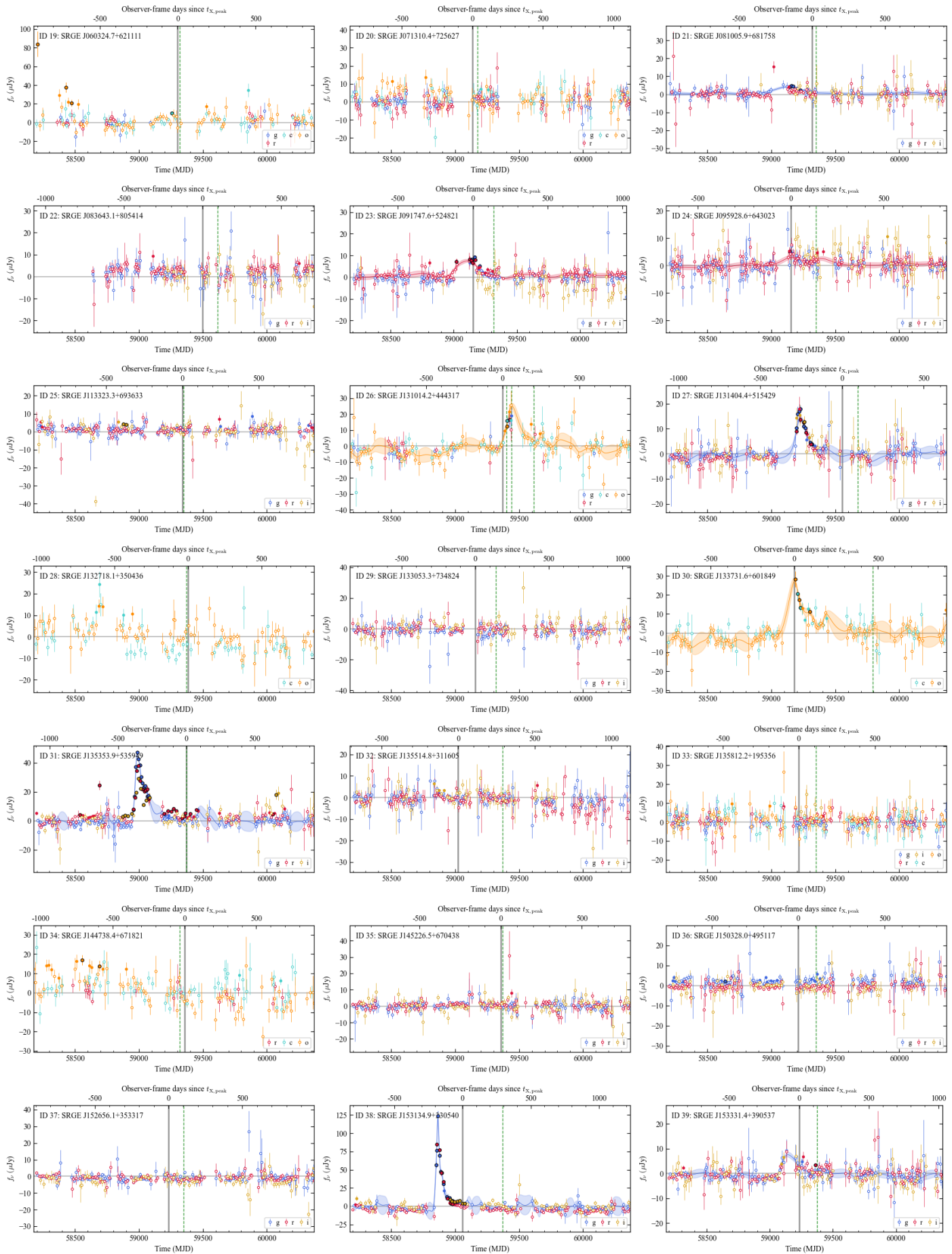


Fig. A.4: Continued figure of Fig. A.3.

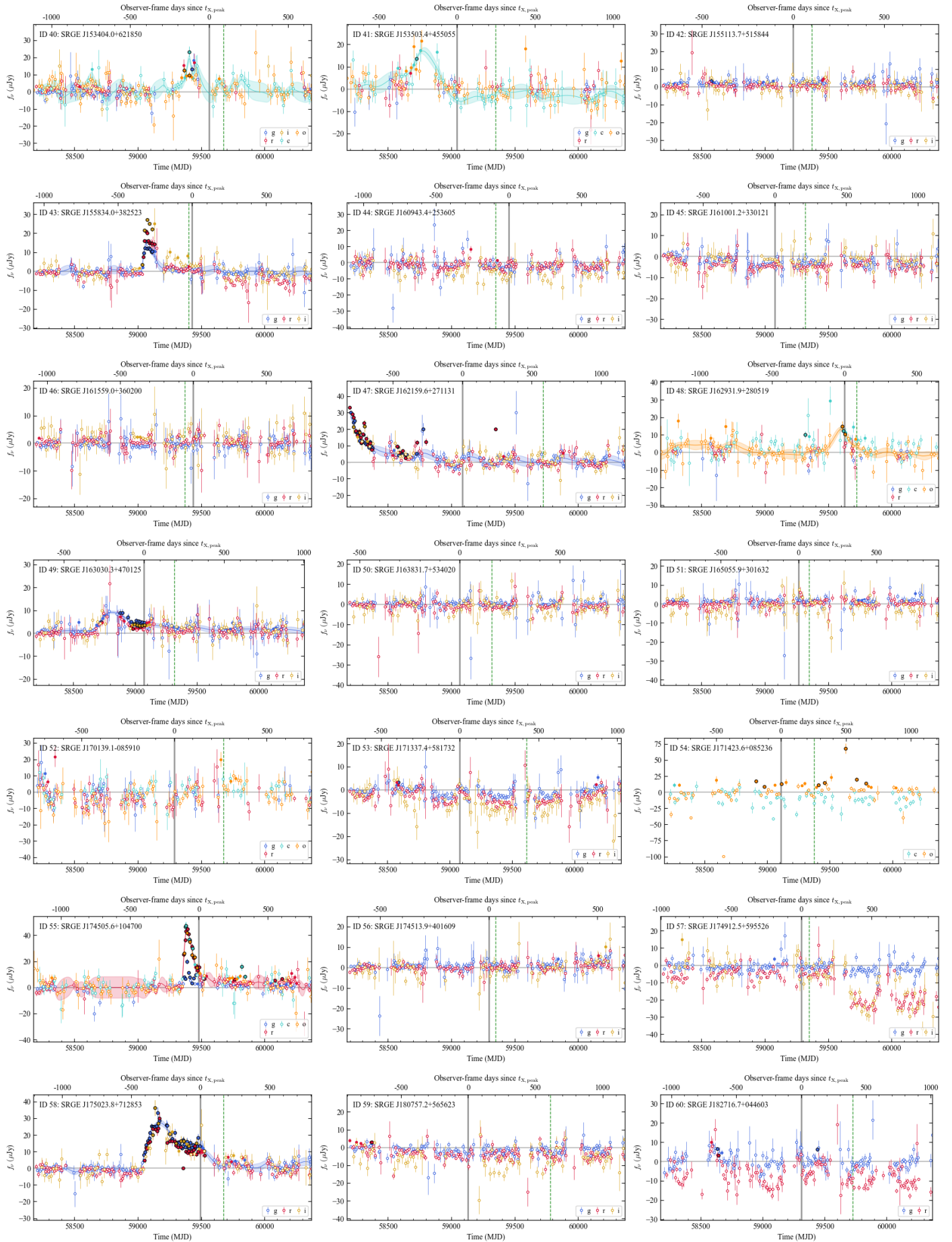
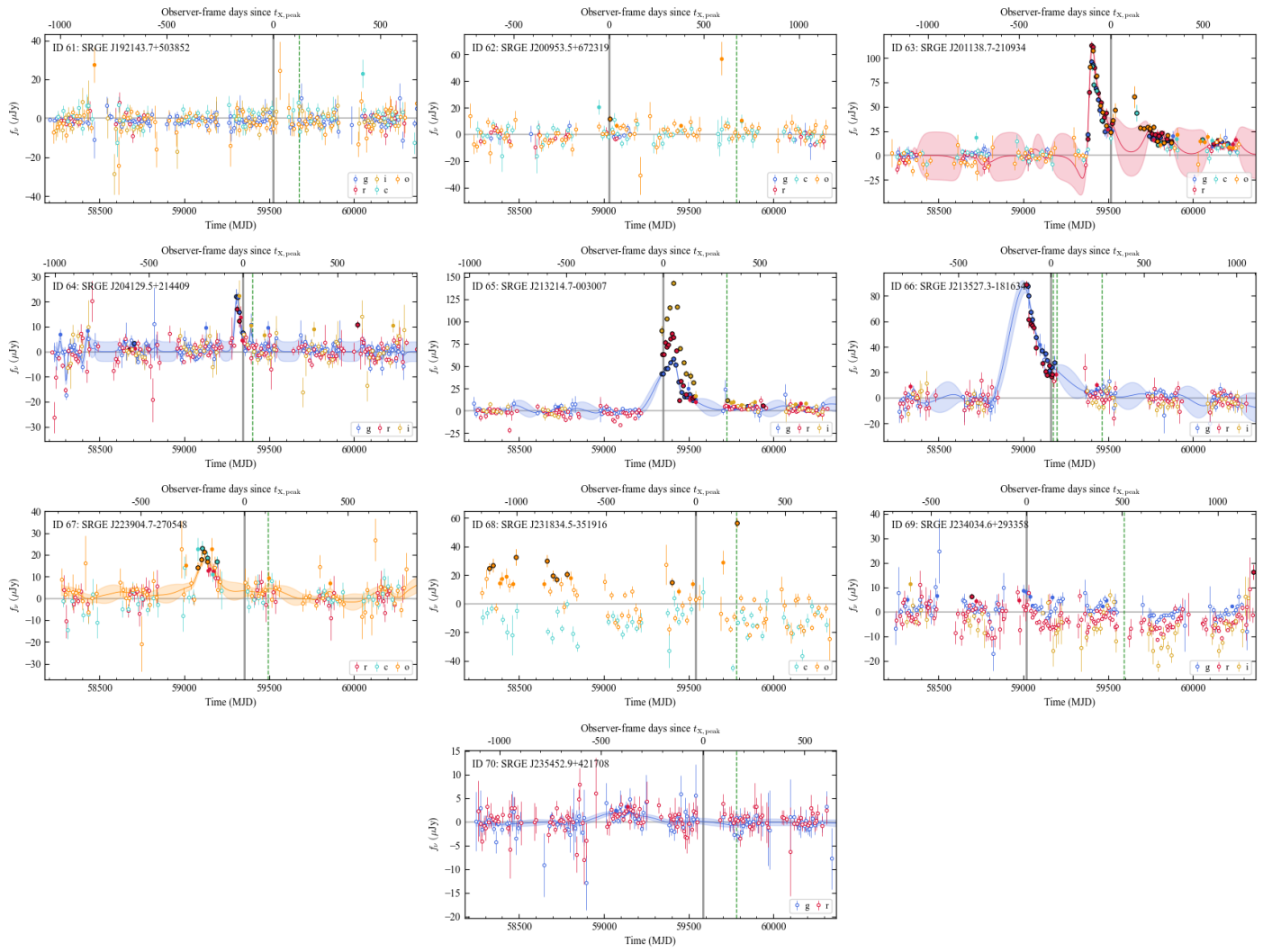
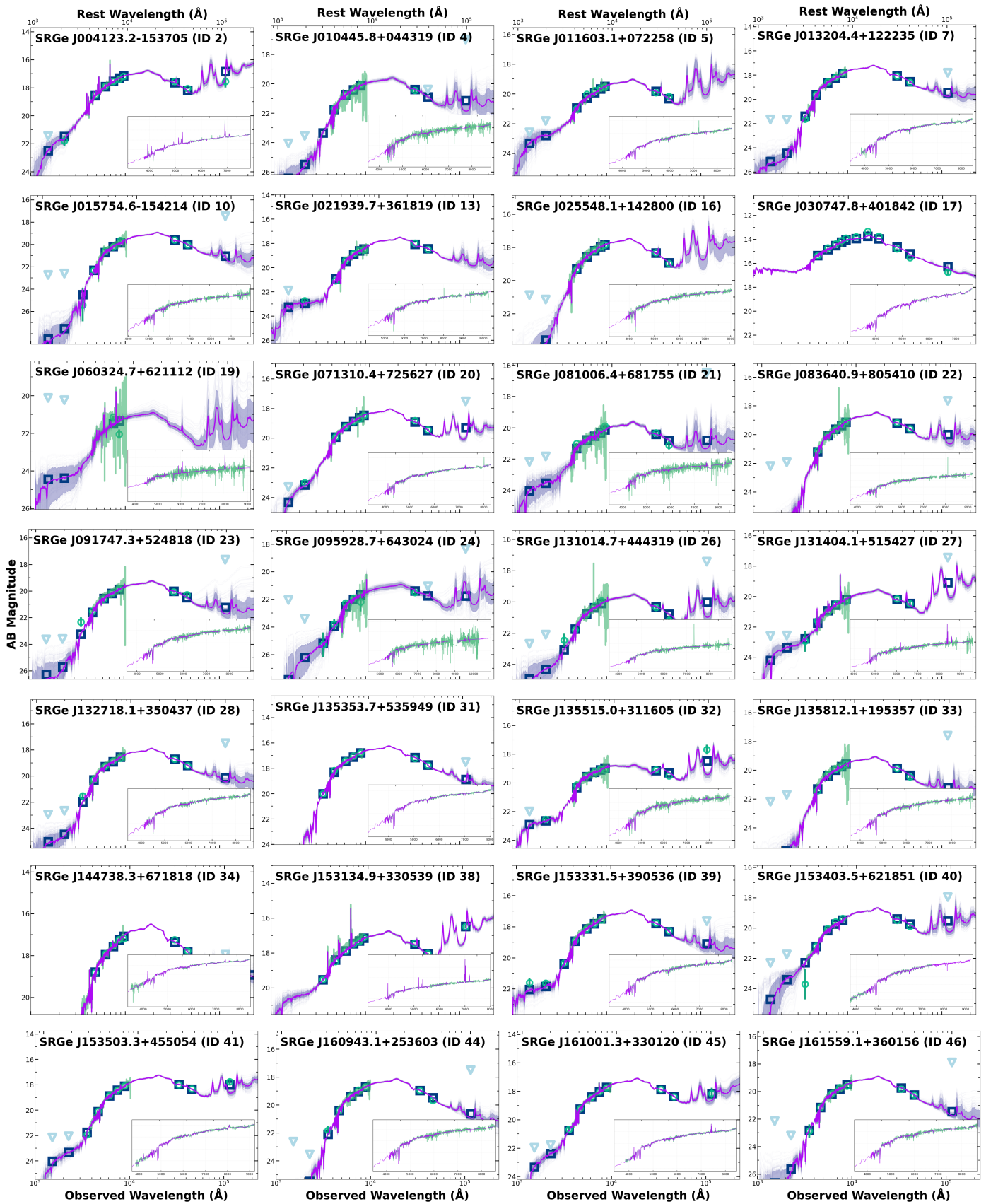


Fig. A.5: Continued figure of Fig. A.4.



**Fig. A.6:** Continued figure of Fig. A.5.



**Fig. A.7:** Prospector SED fitting results for our gold and silver sample, and we show the gold sample first. Observed photometry (green circles), upper limits (light blue triangles), and model spectra (purple lines with gray  $1\sigma$  uncertainty bands) are shown. The inset zooms into the rest-frame 3000-7500 Å region (lower axis: observed frame; upper axis: rest frame). SRGe J163831.9+534018 (ID 50) uses photometry-only fitting due to spectroscopic convergence failure.

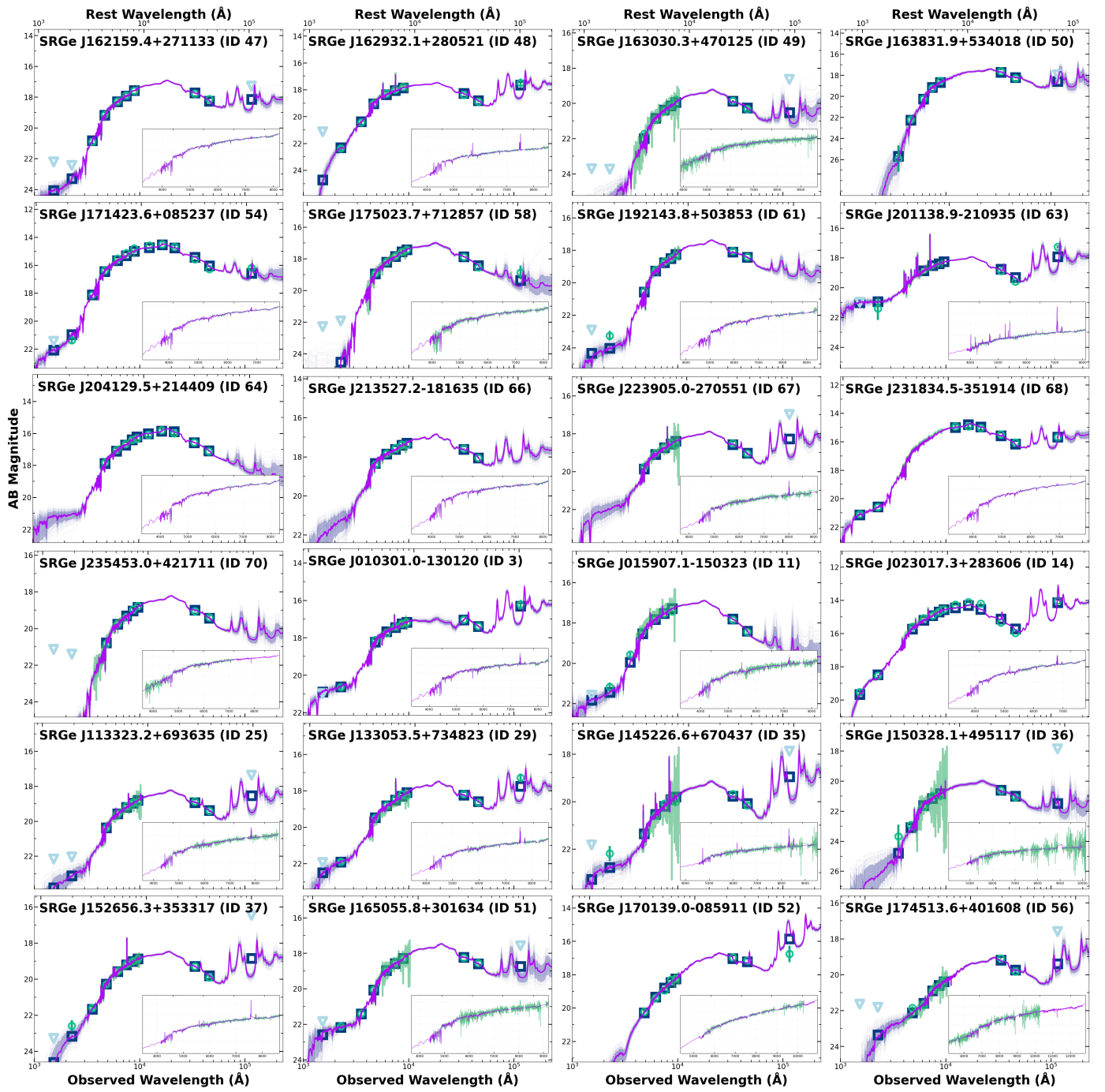


Fig. A.8: Continued figure of Fig. A.7.